Received: 28 January 2017 | Revised: 12 May 2017 | Accepted: 16 May 2017

DOI: 10.1002/nme.5590

RESEARCH ARTICLE

WILEY

Strain localization in a solid-water-air system with random heterogeneity via stabilized mixed finite elements

Xiaoyu Song[1] | Ming Ye[2] | Kaiqi Wang[1]

[1]Department of Civil and Coastal Engineering, University of Florida, 365 Weil Hall Gainesville, FL 32611, USA

[2]Department of Scientific Computing, The Florida State University, Tallahasssee, FL 32306, USA

Correspondence
Xiaoyu Song, Department of Civil and Coastal Engineering, University of Florida, 365 Weil Hall, Gainesville, FL 32611, USA.
Email: xiaoyu.song@essie.ufl.edu

Summary

Unsaturated soils are solid-water-air systems that include a solid skeleton, pore water, and pore air. Heterogeneities in porosity or degree of saturation are salient features of unsaturated soils. These heterogeneities may trigger localized deformation (eg, shear banding) in such materials as demonstrated by numerical simulations via a pseudo three-phase model. In this article, we formulate a true three-phase mathematical framework implemented via stabilized low-order mixed finite elements. With this mathematical framework, we study the evolution of pore air pressure and its role in the inception of strain localization triggered by initial heterogeneity either in porosity or suction. The numerical simulations show that pore air pressure is nonzero and nonuniform in the process of progressive failure in unsaturated soils. The heterogeneity of pore air pressure may also play a significant role in the onset of localized deformation of unsaturated soils. Therefore, a three-phase model considering the pore air phase is physically more appropriate for modeling strain localization in unsaturated soils.

KEYWORDS

heterogeneity, low-order, mixed finite element, porous media, strain localization, stabilized, three-phase

1 | INTRODUCTION

The coupled solid-liquid-air phenomenon exists in multiphase porous media, such as wet clay, sand, and biological tissues (eg, skins and bones).[1-3] Unsaturated soils are three-phase porous media comprising a solid skeleton, pore water, and pore air. The difference between pore air pressure and pore water pressure is called suction. The relationship between suction and degree of saturation is called soil water characteristic curve. Both suction and degree of saturation dramatically impact the mechanical and hydraulic properties (eg, shear strength and permeability) of partially saturated soils.[4] For example, the heterogeneity of suction and degree of saturation in unsaturated soils may trigger localized deformation in unsaturated soils.[5-10] However, these studies assume that the pore air pressure is passive (ie, constant atmospheric pressure). Therefore, the study could not predict the variation of pore air pressure and its potential impact on the inception of localized deformation. However, the pore gas phase plays an important role in the hydromechanical behavior of multiphase deformable porous media.[11-14] A pseudo two-phase formulation cannot capture the observed physical phenomena as a three-phase formulation does, for example, draining process of unsaturated soil samples[15,16] and vapour pressure below the saturation water pressure.[13] In this paper, we study the evolution of heterogeneous pore air phase and its potential impact on the inception of strain localization and progressive failures of

unsaturated soils via a stabilized low-order mixed finite element formulation. Specifically, heterogeneity of the suction field and of dry density has been taken into account and plays a substantial role in triggering localized deformations in unsaturated soils as demonstrated by the numerical examples.

Strain localization is a ubiquitous failure mode of geomaterials. In localized deformation zone, geomaterials involve intense shear deformation that usually serves as a precursor of failure of such materials.[17,18] For this reason, numerous theoretical, experimental, and computational research has been conducted to study the inception of localized deformation and its triggering mechanism in geomaterials under the dry or fluid saturated conditions.[18-33] For example, in Rudnicki and Rice,[19] the authors first derived a mathematical condition of the onset of shear banding in pressure-sensitive geomaterials. Recently, this mathematical criterion has been extended to study the drained bifurcation condition,[9,34,35] and transient bifurcation condition at finite strain[10] for unsaturated soils. The numerical results demonstrated that the spatial variations of density and fluid saturation have a major influence on the inception of localized deformation in unsaturated soils. Researchers also investigated the bifurcation of unsaturated geomaterials at the material point level via constitutive modeling.[36-38]

While theoretical and experimental methods have provided insights into the localized deformation in multiphase geomaterials, computational modeling (eg, the mixed finite element method) is equally useful to study the onset and fundamental triggering mechanism of localized deformation in such materials.[9,13,16,27,39-43] For example, in Callari et al,[40] the authors studied the localized deformation in unsaturated porous media via the finite element enhanced by strong discontinuities method that could resolve the pathological or mesh sensitivity issue with the finite element method.[22] A two-scale model was formulated to study fluid flow in an unsaturated and progressively fracturing porous medium.[44,45] In Lazari et al,[41] the authors formulated a nonlocal constitutive model to simulate localized deformation in unsaturated soil under the nonisothermal conditions. Few of the above numerical formulation considered the spatially varying material properties such as density and fluid saturation and their impacts on the inception of localized deformation in multiphase porous media. Recent numerical investigations of localized failure of unsaturated porous media via a "meso"-scale finite element method have demonstrated that the material heterogeneities, such as density and degree of saturation, have a first-order triggering role in strain localization in unsaturated porous medium.[5-10,46] However, the study above was based on a numerical framework that assumes a passive pore air pressure. Therefore, it cannot capture the active role of gas movement and its impact on progressive failures in solid-water-air systems, such as landfill slope failures.[47]

In this article, we formulate a three-phase computational framework to study the evolution of pore gas pressure and the role of solid-water-air coupling on the inception of localized deformation in unsaturated soils. This computational framework consists of the momentum balance of the mixture, the mass balance equations of pore water and pore air, respectively. To complete the computational model, we will adopt a "meso"-scale constitutive model for the solid skeleton under the isothermal conditions,[8] a soil-water characteristic curve,[48] and the generalized Darcy's law for the flow of pore water and pore air in the connected pore space.[1] The three-phase balance equations are implemented via stabilized low-order mixed finite elements[8,49-51] that allow equal order interpolations of displacement and pore pressure fields for its simplicity and computational efficiency[52] (see subsection 2.5 for more discussions). The numerical simulations conducted in this article are focused on the inception of localized deformation. The numerical results show that the pore gas pressure varies nonuniformly in the problem domain. The comparison of results obtained by the three-phase formulation and the two-phase formulation demonstrates that the former is physically more appropriate to capture localized deformation in unsaturated soils triggered by material heterogeneity either in density or suction. For a physically more appropriate postlocalization analysis of unsaturated porous media, enhancements such as strong discontinuities or the extended finite element technique[28,40,45] may be required to regularize the present numerical formulation at both levels of the finite element and the material model (damage or softening plasticity model),[23,51,53] which is an ongoing effort of the authors.

The remaining part of this article is organized as follows. Section 2 introduces the balance equations, their strong forms, and weak forms, the generalized Darcy's law for pore air and pore water flow and their linearization, stabilized finite element formulation of the weak forms, discretization in finite element space and a global tangent operator. Section 3 presents a "meso"-scale constitutive model for unsaturated soils and a soil-water characteristic curve. Section 4 presents the numerical simulations via the three-phase formulation, the comparison of results with the ones obtained by the equivalent two-phase formulation (ie, assume passive atmospheric pressure), and mesh sensitivity analysis. Section 5 summarizes the conclusion of this article. As for notations and symbols used in this article, bold-faced letters denote tensors and vectors; the symbol "." denotes an inner product of 2 vectors; the symbol ":" denotes an inner product of 2 second-order tensors or double contraction of adjacent indices of tensors of rank 2 or higher; the symbol "$\otimes$" denotes a juxtaposition. For any symmetric second-order tensors $\boldsymbol{\alpha}$ and $\boldsymbol{\beta}$, $(\boldsymbol{\alpha} \otimes \boldsymbol{\beta})_{ijkl} = \alpha_{ij}\beta_{kl}$.

2 | BALANCE EQUATIONS

2.1 | Continuous porous media theory

Continuum porous media theory is formulated on the basis of 2 fundamental hypotheses that the porous medium can be considered as the superposition of several continua that move with distinct kinematics, and the physics of the superposed fluid and solid continua can be described with respect to the initial configuration of the solid phase.[1,54] Following the continuum porous media theory, let ϕ be the porosity of the three-phase porous media, S_r be the degree of saturation of water in the pore space, and $1 - S_r$ be the degree of saturation of air in the pore space. Furthermore, let ρ_s, ρ_w, and ρ_a be the intrinsic density of soil grains, pore water, and pore air, respectively. Therefore, the density of the mixture reads

$$\rho = (1 - \phi)\rho_s + \phi S_r \rho_w + \phi(1 - S_r)\rho_a. \tag{1}$$

To model the deformation of a porous medium, we need to define an effective stress for the solid skeleton that serves to transfer the multiphase material into an equivalent single-phase material. For partially saturated soils, there are 2 kinds of stress tensors for constitutive modeling of the solid phase. In the first one, the total stress tensor is decomposed into net stress (ie, total stress minus pore air pressure) and suction (ie, pore air pressure minus pore water pressure) multiplied by the second-order identity tensor. In the second type, the generalized Bishop-type effective stress tensor is used to model the stress state of the solid phase. It is worth noting that the Bishop effective stress tensor is the energy conjugate of the strain of the solid skeleton.[55] The authors admit that it is an arguable topic on which effective stress should be used to model unsaturated soils. However, there may be several advantages with the adoption of the Bishop-type effective stress although the selection of which stress tensor mostly depends on the convenience as stated in Nuth and Laloui.[56] For example, when the Bishop-type effective stress is adopted, the critical state line may be unique for the same soils under both saturated and unsaturated conditions. Without loss of the generality, here, we adopt the generalized Bishop-type effective stress following the convention in continuum mechanics (ie, negative stress means compression).[57]

$$\boldsymbol{\sigma} = \boldsymbol{\sigma}' - B\left[S_r p_w + (1 - S_r)p_a\right]\boldsymbol{I}, \tag{2}$$

where $\boldsymbol{\sigma}$ is the total Cauchy stress tensor, $\boldsymbol{\sigma}'$ is the effective Cauchy stress that is energy conjugate to the rate of deformation of the solid matrix, $\mathbf{1}$ is the second-order identity tensor, p_w and p_a are pore water pressure and pore air pressure, respectively, and B is the Biot coefficient that is assumed to be 1 for soils[55] in this article.

2.2 | Strong forms

In this article, we assume that the basic unknowns for the three-phase mixture are the displacement of the solid phase $\boldsymbol{u}$, pore water pressure p_w, and pore air pressure p_a. Furthermore, we assume that the solid skeleton and the pore water are incompressible. For the air phase, we assume that the ideal gas law applies,

$$\rho_a = \frac{p_a M_a}{RT}, \tag{3}$$

where M_a is the molar mass of air, R is the universal gas constant, and T is the absolute temperature (ie, the environmental temperature under an isothermal condition). The bulk modulus of pore air pressure is assumed to be pore air pressure, that is, $K_a = p_a$.[34] Following the continuous porous media theory, the momentum balance equation for the mixture can be written as

$$\boldsymbol{\nabla} \cdot \left[\boldsymbol{\sigma}' - S_r p_w \boldsymbol{I} - (1 - S_r)p_a \boldsymbol{I}\right] + \rho \boldsymbol{g} = 0, \tag{4}$$

where $\boldsymbol{\nabla}$ is the spatial gradient operator and $\boldsymbol{g}$ is the gravity acceleration vector. We focus on the current configuration of the three-phase mixture and describe the motions of pore water and pore air following the motion of the solid phase. Then, we can write the mass balance equations of the pore water phase and the pore air phase as follows,[7,8,34]

$$S_r \boldsymbol{\nabla} \cdot \dot{\boldsymbol{u}} - \phi \frac{\partial S_r}{\partial s}\dot{p}_w + \phi \frac{\partial S_r}{\partial s}\dot{p}_a + \frac{1}{\rho_w}\boldsymbol{\nabla} \cdot (\rho_w \bar{\boldsymbol{v}}^w) = 0, \tag{5}$$

$$(1 - S_r)\boldsymbol{\nabla} \cdot \dot{\boldsymbol{u}} + \phi \frac{\partial S_r}{\partial s}\dot{p}_w + \left(\frac{\phi(1 - S_r)}{K_a} - \phi \frac{\partial S_r}{\partial s}\right)\dot{p}_a + \frac{1}{\rho_a}\boldsymbol{\nabla} \cdot (\rho_a \bar{\boldsymbol{v}}^a) = 0, \tag{6}$$

where $\bar{\boldsymbol{v}}^w$ and $\bar{\boldsymbol{v}}^a$ are Darcy velocities of pore water and pore air, respectively.

We assume that the three-phase mixture occupies a domain $\mathcal{B}$ with a boundary Γ. The boundary Γ is decomposed into the regions where essential and natural boundary conditions are specified for the solid skeleton and pore fluids. Specifically, we define that Γ_u and Γ_t are solid displacement and solid traction boundaries, respectively; Γ_{p_w} and Γ_{q_w} are pore water pressure and pore water flux boundaries respectively; and Γ_{p_a} and Γ_{q_a} are pore air pressure and pore air flux boundaries, respectively. This decomposition is subject to the following restrictions,

$$\Gamma = \Gamma_u \cup \Gamma_t = \Gamma_{p_w} \cup \Gamma_{q_w} = \Gamma_{p_a} \cup \Gamma_{q_a}, \tag{7}$$

$$\Gamma_u \cup \Gamma_t = \Gamma_{p_w} \cap \Gamma_{q_w} = \Gamma_{p_a} \cap \Gamma_{q_a} = \emptyset. \tag{8}$$

The corresponding boundary conditions are prescribed as

$$\boldsymbol{u} = \overline{\boldsymbol{u}} \text{ on } \Gamma_u, \text{ and } \boldsymbol{n} \cdot \boldsymbol{\sigma}' = \bar{\boldsymbol{t}} \text{ on } \Gamma_t, \tag{9}$$

$$p_w = \bar{p}_w \text{ on } \Gamma_{p_w}, \text{ and } -\boldsymbol{n} \cdot \overline{\boldsymbol{v}}^w = \bar{q}_w \text{ on } \Gamma_{q_w}, \tag{10}$$

$$p_a = \bar{p}_a \text{ on } \Gamma_{p_a}, \text{ and } -\boldsymbol{n} \cdot \overline{\boldsymbol{v}}^a = \bar{q}_a \text{ on } \Gamma_{q_a}, \tag{11}$$

where $\boldsymbol{n}$ is the normal to the boundary surface. And the initial conditions at $t = 0$ are prescribed as $\{\boldsymbol{u}_0, p_{w0}, p_{a0}\}$.

2.3 | Weak forms

To obtain the weak form of the boundary value problem, we first define three spaces of trial functions,

$$\mathcal{S}_u = \left\{ \boldsymbol{u} : \mathcal{B} \to \mathcal{R}^3 | \boldsymbol{u} \boldsymbol{n} \mathcal{H}^1, \boldsymbol{u} = \overline{\boldsymbol{u}} \text{ on } \Gamma_u \right\}, \tag{12}$$

$$\mathcal{S}_{p_w} = \left\{ p_w : \mathcal{B} \to \mathcal{R} | p_w \in \mathcal{H}^1, p_w = \bar{p}_w \text{ on } \Gamma_{p_w} \right\}, \tag{13}$$

$$\mathcal{S}_{p_a} = \left\{ p_a : \mathcal{B} \to \mathcal{R} | p_a \in \mathcal{H}^1, p_a = \bar{p}_a \text{ on } \Gamma_{p_a} \right\}, \tag{14}$$

where $\mathcal{H}^1$ represents a Sobolev space of degree one. The corresponding variational spaces with homogeneous essential boundaries are

$$\mathcal{V}_u = \left\{ \boldsymbol{\eta} : \mathcal{B} \to \mathcal{R}^3 | \boldsymbol{\eta} \in \mathcal{H}^1, \boldsymbol{\eta} = \boldsymbol{0} \text{ on } \Gamma_u \right\}, \tag{15}$$

$$\mathcal{V}_{p_w} = \left\{ \vartheta_w : \mathcal{B} \to \mathcal{R} | \vartheta_w \in \mathcal{H}^1, \vartheta_w = 0 \text{ on } \Gamma_{p_w} \right\}, \tag{16}$$

$$\mathcal{V}_{p_a} = \left\{ \vartheta_a : \mathcal{B} \to \mathcal{R} | \vartheta_a \in \mathcal{H}^1, \vartheta_a = 0 \text{ on } \Gamma_{p_a} \right\}. \tag{17}$$

The weak form of this boundary value problem is then to find $\{\boldsymbol{u}, p_w, p_a\} \in \mathcal{S}_{\boldsymbol{u}} \times \mathcal{S}_{p_w} \times \mathcal{S}_{p_a}$ such that for all $\{\boldsymbol{\eta}, \vartheta_w, \vartheta_a\} \in \mathcal{V}_{\boldsymbol{u}} \times \mathcal{V}_{p_w} \times \mathcal{V}_{p_a}$,

$$\mathcal{G} = 0, \ \widetilde{\mathcal{M}}_w = 0, \text{ and } \widetilde{\mathcal{M}}_a = 0, \tag{18}$$

where

$$\mathcal{G} = \int_{\mathcal{B}} \boldsymbol{\nabla}^s \boldsymbol{\eta} : \left[\boldsymbol{\sigma}' - S_r p_w \boldsymbol{1} - (1 - S_r) p_a \boldsymbol{1} \right] \mathrm{d}V - \int_{\mathcal{B}} \boldsymbol{\eta} \cdot \rho \boldsymbol{g} \mathrm{d}V - \int_{\Gamma_t} \boldsymbol{\eta} \cdot \bar{\boldsymbol{t}} \mathrm{d}A, \tag{19}$$

$$\widetilde{\mathcal{M}}_w = \int_{\mathcal{B}} \vartheta_w \left[S_r \boldsymbol{\nabla} \cdot \dot{\boldsymbol{u}} - \phi \frac{\partial S_r}{\partial s} \dot{p}_w + \phi \frac{\partial S_r}{\partial s} \dot{p}_a \right] \mathrm{d}V - \int_{\mathcal{B}} \boldsymbol{\nabla} \vartheta_w \cdot \overline{\boldsymbol{v}}^w \mathrm{d}V - \int_{\Gamma_{q_w}} \vartheta_w \bar{q}_w \mathrm{d}A, \tag{20}$$

$$\begin{aligned} \widetilde{\mathcal{M}}_a = & \int_{\mathcal{B}} \vartheta_a \left[(1 - S_r) \boldsymbol{\nabla} \cdot \dot{\boldsymbol{u}} + \phi \frac{\partial S_r}{\partial s} \dot{p}_w + \left(\frac{\phi (1 - S_r)}{K_a} - \phi \frac{\partial S_r}{\partial s} \right) \dot{p}_a \right] \mathrm{d}V \\ & - \int_{\mathcal{B}} \boldsymbol{\nabla} \vartheta_a \cdot \overline{\boldsymbol{v}}^a \mathrm{d}V - \int_{\Gamma_{q_a}} \vartheta_a \bar{q}_a \mathrm{d}A. \end{aligned} \tag{21}$$

Motivated by the return mapping algorithm[58] that uses the standard backward implicit scheme for a stress-point integration, we adopt the backward implicit scheme to integrate the variational forms of the mass balance equations of pore water and pore air. Let Δt be the time increment, at time step $n + 1$; we have

$$\mathscr{M}_w = \int_{\mathcal{B}} \vartheta_w \left[S_r \boldsymbol{\nabla} \cdot \Delta \boldsymbol{u} - \phi \frac{\partial S_r}{\partial s} \Delta p_w + \phi \frac{\partial S_r}{\partial s} \Delta p_a \right] \mathrm{d}V - \Delta t \int_{\mathcal{B}} \boldsymbol{\nabla} \vartheta_w \cdot \overline{\boldsymbol{v}}^w \mathrm{d}V - \Delta t \int_{\Gamma_{q_w}} \vartheta_w \bar{q}_w \mathrm{d}A, \tag{22}$$

$$\begin{aligned} \mathscr{M}_a = & \int_{\mathcal{B}} \vartheta_a \left[(1 - S_r) \boldsymbol{\nabla} \cdot \Delta \boldsymbol{u} + \phi \frac{\partial S_r}{\partial s} \Delta p_w \right] \mathrm{d}V + \int_{\mathcal{B}} \vartheta_a \left(\frac{\phi(1 - S_r)}{K_a} - \phi \frac{\partial S_r}{\partial s} \right) \Delta p_a \mathrm{d}V \\ & - \Delta t \int_{\mathcal{B}} \boldsymbol{\nabla} \vartheta_a \cdot \overline{\boldsymbol{v}}^a \mathrm{d}V - \Delta t \int_{\Gamma_{q_a}} \vartheta_a \bar{q}_a \mathrm{d}A, \end{aligned} \tag{23}$$

where $\Delta \boldsymbol{u} = \boldsymbol{u}_{n+1} - \boldsymbol{u}_n$, $\Delta p_w = p_{w,n+1} - p_{w,n}$, and $\Delta p_a = p_{a,n+1} - p_{a,n}$. Next, we conduct the variations on the momentum balance and the mass balance equations of pore water and pore air, respectively. For the momentum balance equation, its variational form can be written as

$$\delta \mathscr{G} = \int_{\mathcal{B}} \boldsymbol{\nabla}^s \boldsymbol{\eta} : \left[\frac{\partial \boldsymbol{\sigma}'}{\partial \boldsymbol{\nabla}^s \boldsymbol{u}} : \boldsymbol{\nabla}^s \delta \boldsymbol{u} + \frac{\partial \boldsymbol{\sigma}'}{\partial s} \delta s - \overline{S_r} \boldsymbol{I} \delta p_w + (\overline{S_r} - 1) \boldsymbol{I} \delta p_a \right] \mathrm{d}V - \int_{\mathcal{B}} \boldsymbol{\eta} \cdot \boldsymbol{g} \delta \rho \mathrm{d}V, \tag{24}$$

where $\overline{S_r} = \frac{\partial S_r}{\partial s} s + S_r$, and assuming that air is weightless, $\delta \rho = \rho_w \phi \frac{\partial S_r}{\partial s} (\delta p_a - \delta p_w)$ for an infinitesimal deformation. The variational form of the balance of the water phase for a fixed surface flux of pore water is

$$\delta \mathscr{M}_w = \int_{\mathcal{B}} \vartheta_w \left[S_r \boldsymbol{\nabla} \cdot \delta \boldsymbol{u} - \tilde{\phi} \frac{\partial S_r}{\partial s} \delta p_w \right] \mathrm{d}V + \int_{\mathcal{B}} \vartheta_w \tilde{\phi} \frac{\partial S_r}{\partial s} \delta p_a \mathrm{d}V - \Delta t \int_{\mathcal{B}} \boldsymbol{\nabla} \vartheta_w \cdot \delta \overline{\boldsymbol{v}}^w \mathrm{d}V, \tag{25}$$

where $\tilde{\phi} = \boldsymbol{\nabla} \cdot \Delta \boldsymbol{u} + \phi$. Similarly, the variational form of the balance equation of the air phase for a fixed surface flux of pore air can be written as

$$\begin{aligned} \delta \mathscr{M}_a = & \int_{\mathcal{B}} \vartheta_a \left[(1 - S_r) \boldsymbol{\nabla} \cdot \delta \boldsymbol{u} + \left(\tilde{\phi} + \frac{\phi}{K_a} \Delta p_a \right) \frac{\partial S_r}{\partial s} \delta p_w \right] \mathrm{d}V \\ & + \int_{\mathcal{B}} \vartheta_a \left[\frac{\phi(1 - S_r)}{K_a} - \left(\tilde{\phi} + \frac{\phi}{K_a} \Delta p_a \right) \frac{\partial S_r}{\partial s} \right] \delta p_a \mathrm{d}V - \Delta t \int_{\mathcal{B}} \boldsymbol{\nabla} \vartheta_a \cdot \delta \overline{\boldsymbol{v}}^a \mathrm{d}V. \end{aligned} \tag{26}$$

2.4 | Generalized Darcy's law for water and air

The pore water flow and pore air flow can be described by the generalized Darcy's law[54,59] as follow:

$$\overline{\boldsymbol{v}}^w = -k_{rw} \boldsymbol{k}_{\mathrm{w}} \cdot (\boldsymbol{\nabla} p_w + \rho_w \boldsymbol{g}), \tag{27}$$

$$\overline{\boldsymbol{v}}^a = -k_{ra} \boldsymbol{k}_{\mathrm{a}} \cdot (\boldsymbol{\nabla} p_a + \rho_a \boldsymbol{g}), \tag{28}$$

where $\boldsymbol{k}_w = k_w \mathbf{1}$ and $\boldsymbol{k}_a = k_a \mathbf{1}$ are the intrinsic permeabilities of pore water and pore air in the solid, respectively; k_{rw} and k_{ra} are the relative permeabilities related to the pore water phase and the pore air phase, respectively. Both relative permeabilities are dependent on the effective degree of saturation that is defined in the next section. With the generalized Darcy's law at hand, we can write out the variational forms of flux terms in Equations 25 and 26 as follows:

$$\delta \overline{\boldsymbol{v}}^w = -k_{rw} \boldsymbol{k}_w \cdot \boldsymbol{\nabla} \delta p_w - \left[\boldsymbol{k}_w \cdot (\boldsymbol{\nabla} p_w + \rho_w \boldsymbol{g}) \right] \frac{\partial k_{rw}}{\partial s} (\delta p_a - \delta p_w), \tag{29}$$

$$\delta \overline{\boldsymbol{v}}^a = -k_{ra} \boldsymbol{k}_a \cdot \boldsymbol{\nabla} \delta p_a - \left[\boldsymbol{k}_a \cdot (\boldsymbol{\nabla} p_a + \rho_a \boldsymbol{g}) \right] \frac{\partial k_{ra}}{\partial s} (\delta p_a - \delta p_w), \tag{30}$$

where

$$\frac{\partial k_{rw}}{\partial s} = \frac{\partial k_{rw}}{\partial S_r} \frac{\partial S_r}{\partial s}, \text{ and } \frac{\partial k_{ra}}{\partial s} = \frac{\partial k_{ra}}{\partial S_r} \frac{\partial S_r}{\partial s}. \tag{31}$$

Substituting Equations 29 and 30 into the last terms on the right-hand side of Equations 25 and 26 generates,

$$\begin{aligned} -\Delta t \int_{\mathcal{B}} \boldsymbol{\nabla} \vartheta_w \cdot \overline{\boldsymbol{v}}^w \mathrm{d}V = & \Delta t \int_{\mathcal{B}} \boldsymbol{\nabla} \vartheta^w \cdot \left[\boldsymbol{k}_w \cdot (\boldsymbol{\nabla} p_w + \rho_w \boldsymbol{g}) \right] \frac{\partial k_{rw}}{\partial s} (\delta p_a - \delta p_w) \mathrm{d}V \\ & + \Delta t \int_{\mathcal{B}} \boldsymbol{\nabla} \vartheta^w \cdot (k_{rw} \boldsymbol{k}_w) \cdot \boldsymbol{\nabla} \delta p_w \mathrm{d}V, \end{aligned} \tag{32}$$

$$-\Delta t\int_{\mathcal{B}}\boldsymbol{\nabla}\vartheta_a\cdot\bar{\boldsymbol{v}}^a\mathrm{d}V=\Delta t\int_{\mathcal{B}}\boldsymbol{\nabla}\vartheta^a\cdot\left[\boldsymbol{k}_a\cdot(\boldsymbol{\nabla}p_a+\rho_a\boldsymbol{g})\right]\frac{\partial k_{ra}}{\partial s}(\delta p_a-\delta p_w)\mathrm{d}V+\Delta t\int_{\mathcal{B}}\boldsymbol{\nabla}\vartheta^a\cdot(k_{ra}\boldsymbol{k}_a)\cdot\boldsymbol{\nabla}\delta p_a\mathrm{d}V. \tag{33}$$

2.5 | Stabilization formulation for low-order mixed finite elements

In this part, we present stabilized formulations of mass balance equations of pore water and pore air to use a three-phase version of stabilized Q4P4 elements[8,49,50,60-62] instead of Q9P4 elements (eg, the Taylor-Hood element[63]) for two-phase coupled solid deformation-diffusion problems. Here, "Q" refers to the number of solid skeleton displacement nodes, and "P" refers to the number of pore fluid pressure nodes. In this case, for each element, there are 4 nodes and each node has 4 degrees of freedom (2 for displacement, 1 for pore water pressure, and 1 for pore air pressure) under the plane strain condition. The purpose of using stabilized low-order mixed finite elements is twofold. First, from a computation point of view, using low-order mixed finite elements rather than high-order mixed finite elements (eg, the Taylor-Hood elements) to spatially discretize the three-phase field equations dramatically reduces the numerical problem size (ie, the total degree of freedom) that favors large-scale computations. Second, standard low-order mixed finite elements without stabilization (ie, the equal order interpolation of displacement and pore pressure variables) has a notorious instability issue in the form of spurious pressure oscillation, which is generally recognized as the result of the mixed finite elements violating the inf-sup condition.[64-68] Several methods have been formulated to stabilize the low-order mixed finite element, for instance, the Galerkin least-squares method,[69] the variational multiscale technqiue,[70] and the Polynomial-Pressure-Projection (PPP) approach.[71,72] We refer Truty and Zimmermann[73] and Preisig and Prévost[74] for further discussions on this topic.

The formulation here is based on the PPP technique originally developed for Stokes flow[71,72] and later applied to poromechanics problems.[8,49,50,60-62] For the three-phase poromechanics problem, here, the application of the PPP techinque leads to a twofold saddle point problem[75] like the one recently formulated for porous media with double porosity in Choo and Borja.[50] Recall the original PPP technique for two-phase poromechanics with single porosity,[49] and the projection operator for the water and air phases can be written as

$$\Pi p_w|_{\mathcal{B}^e}=\frac{1}{V^e}\int_{\mathcal{B}^e}p_w\mathrm{d}V,\ \text{and}\ \Pi p_a|_{\mathcal{B}^e}=\frac{1}{V^e}\int_{\mathcal{B}^e}p_a\mathrm{d}V, \tag{34}$$

where V^e is the volume of the element. The value of the projected pore water pressure and pore air pressure within each element is simply equal to the element average of p_w and p_a, respectively. The temporal discretized versions of the balance equations of pore water and pore air are modified with additional terms as follows:

$$\mathscr{M}_w+\mathscr{M}_w^{\mathrm{stab}}=0,\ \text{and}\ \mathscr{M}_a+\mathscr{M}_a^{\mathrm{stab}}=0, \tag{35}$$

where

$$\mathscr{M}_w^{\mathrm{stab}}=\int_{\mathcal{B}}\frac{\tau}{2G}(\vartheta_w-\Pi\vartheta_w)(\Delta p_w-\Pi\Delta p_w)\,\mathrm{d}V, \tag{36}$$

$$\mathscr{M}_a^{\mathrm{stab}}=\int_{\mathcal{B}}\frac{\tau}{2G}(\vartheta_a-\Pi\vartheta_a)(\Delta p_a-\Pi\Delta p_a)\,\mathrm{d}V. \tag{37}$$

Here, G is the shear modulus of the solid skeleton and $\tau>0$ is a constant multiplier.[49] Then, we have the variational forms of $\mathscr{M}_w^{\mathrm{stab}}$ and $\mathscr{M}_a^{\mathrm{stab}}$ as follows:

$$\delta\mathscr{M}_w^{\mathrm{stab}}=\int_{\mathcal{B}}\frac{\tau}{2G}(\vartheta_w-\Pi\vartheta_w)(\delta p_w-\Pi\delta p_w)\,\mathrm{d}V, \tag{38}$$

$$\delta\mathscr{M}_a^{\mathrm{stab}}=\int_{\mathcal{B}}\frac{\tau}{2G}(\vartheta_a-\Pi\vartheta_a)(\delta p_a-\Pi\delta p_a)\,\mathrm{d}V. \tag{39}$$

In summary, the variational forms of the momentum balance of the mixture, the pore water mass balance, and the pore air mass balance at time step $n+1$ are as follows :

$$\delta\mathscr{G}=\int_{\mathcal{B}}\boldsymbol{\nabla}^s\boldsymbol{\eta}:\frac{\partial\boldsymbol{\sigma}'}{\partial\boldsymbol{\nabla}^s\boldsymbol{u}}:\boldsymbol{\nabla}^s\delta\boldsymbol{u}\mathrm{d}V+\int_{\mathcal{B}}\boldsymbol{\nabla}^s\boldsymbol{\eta}:\frac{\partial\boldsymbol{\sigma}'}{\partial s}(\delta p_a-\delta p_w)\mathrm{d}V-\int_{\mathcal{B}}\boldsymbol{\nabla}^s\boldsymbol{\eta}:\boldsymbol{1}\overline{S_r}\delta p_w\mathrm{d}V+\int_{\mathcal{B}}\boldsymbol{\nabla}^s\boldsymbol{\eta}:\boldsymbol{1}(\overline{S_r}-1)\delta p_a\mathrm{d}V-\int_{\mathcal{B}}\boldsymbol{\eta}\cdot\boldsymbol{g}\delta\rho\mathrm{d}V, \tag{40}$$

$$\begin{aligned}\delta\mathscr{M}_w = &\int_{\mathcal{B}} \vartheta_w S_r \boldsymbol{\nabla}\cdot\delta\boldsymbol{u}\mathrm{d}V - \int_{\mathcal{B}} \vartheta_w \tilde{\phi}\frac{\partial S_r}{\partial s}\delta p_w \mathrm{d}V - \Delta t\int_{\mathcal{B}} \boldsymbol{\nabla}\vartheta_w\cdot\boldsymbol{k}_w\cdot(\boldsymbol{\nabla}p_w+\rho_w\boldsymbol{g})\frac{\partial k_{rw}}{\partial s}\delta p_w\mathrm{d}V\\ &+\int_{\mathcal{B}}\frac{\tau}{2G}\tilde{\Pi}\vartheta_w\tilde{\Pi}\delta p_w\mathrm{d}V + \Delta t\int_{\mathcal{B}}\boldsymbol{\nabla}\vartheta_w\cdot(k_{rw}\boldsymbol{k}_w)\cdot\boldsymbol{\nabla}\delta p_w\mathrm{d}V\\ &+\int_{\mathcal{B}}\vartheta_w\tilde{\phi}\frac{\partial S_r}{\partial s}\delta p_a\mathrm{d}V + \Delta t\int_{\mathcal{B}}\boldsymbol{\nabla}\vartheta_w\cdot\boldsymbol{k}_w\cdot(\boldsymbol{\nabla}p_w+\rho_w\boldsymbol{g})\frac{\partial k_{rw}}{\partial s}\delta p_a\mathrm{d}V,\end{aligned} \tag{41}$$

$$\begin{aligned}\delta\mathscr{M}_a = &\int_{\mathcal{B}}\vartheta_a(1-S_r)\boldsymbol{\nabla}\cdot\delta\boldsymbol{u}\mathrm{d}V + \int_{\mathcal{B}}\vartheta_a\left(\tilde{\phi}+\frac{\phi}{K_a}\Delta p_a\right)\frac{\partial S_r}{\partial s}\delta p_w\mathrm{d}V\\ &-\Delta t\int_{\mathcal{B}}\boldsymbol{\nabla}\vartheta_a\cdot\boldsymbol{k}_a\cdot\boldsymbol{\nabla}p_a\frac{\partial k_{ra}}{\partial s}\delta p_w\mathrm{d}V + \int_{\mathcal{B}}\vartheta_a\left[\frac{\phi(1-S_r)}{K_a}-\left(\tilde{\phi}+\frac{\phi}{K_a}\Delta p_a\right)\frac{\partial S_r}{\partial s}\right]\delta p_a\mathrm{d}V\\ &+\Delta t\int_{\mathcal{B}}\boldsymbol{\nabla}\vartheta_a\cdot\boldsymbol{k}_a\cdot\boldsymbol{\nabla}p_a\frac{\partial k_{ra}}{\partial s}\delta p_a\mathrm{d}V + \int_{\mathcal{B}}\frac{\tau}{2G}\tilde{\Pi}\vartheta_a\tilde{\Pi}\delta p_a\mathrm{d}V\\ &+\Delta t\int_{\mathcal{B}}\boldsymbol{\nabla}\vartheta_a\cdot(k_{ra}\boldsymbol{k}_a)\cdot\boldsymbol{\nabla}\delta p_a\mathrm{d}V.\end{aligned} \tag{42}$$

Here, the operator $\tilde{\Pi} = 1-\Pi$ and Π is defined in Equation 34. Note that the constitutive model for the solid phase and a soil-water characteristic curve will be introduced in Section 3.

2.6 | Discretization in the mixed finite element spaces and the global tangent operator

The basic variables in this formulation are displacements of the solid skeleton $\boldsymbol{u}$, pore water pressure p_w, and pore air pressure p_a. The weighting functions and the solutions of $\boldsymbol{u}$, p_w, and p_a are expressed in terms of their of nodal values as

$$\boldsymbol{\eta} = \boldsymbol{N}_u\boldsymbol{c}_u, \qquad \text{and } \boldsymbol{u} = \boldsymbol{N}_u\boldsymbol{u}, \tag{43}$$

$$\vartheta_w = \boldsymbol{N}_w\boldsymbol{c}_w, \qquad \text{and } p_w = \boldsymbol{N}_w\boldsymbol{p}_w, \tag{44}$$

$$\vartheta_a = \boldsymbol{N}_a\boldsymbol{c}_a, \qquad \text{and } p_a = \boldsymbol{N}_a\boldsymbol{p}_a, \tag{45}$$

where $\boldsymbol{N}_u$, $\boldsymbol{N}_w$, and $\boldsymbol{N}_a$ are the global shape functions for the displacement of the solid skeleton, pore water pressure and pore air pressure, respectively. $\boldsymbol{c}_u$, $\boldsymbol{c}_w$, and $\boldsymbol{c}_a$ are vectors of the variations of the displacement of the solid skeleton, pore water pressure and pore air pressure, respectively. $\boldsymbol{u}$, $\boldsymbol{p}_w$, and $\boldsymbol{p}_a$ are vectors of the solutions of the displacement of the solid skeleton, pore water pressure, and pore air pressure, respectively. Let

$$\boldsymbol{B} = \boldsymbol{\nabla}^s\boldsymbol{N}_u,\ \boldsymbol{b} = \boldsymbol{\nabla}\cdot\boldsymbol{N}_u,\ \boldsymbol{E}_w = \boldsymbol{\nabla}\boldsymbol{N}_w,\ \text{and } \boldsymbol{E}_a = \boldsymbol{\nabla}\boldsymbol{N}_a. \tag{46}$$

Then, the application of standard finite element discretisation procedure[76] results in the following 3 balance equations at time step $n+1$,

$$\int_{\mathcal{B}}\boldsymbol{B}^T\left[\boldsymbol{\sigma}' - S_r p_w\boldsymbol{I} - (1-S_r)p_a\boldsymbol{I}\right]\mathrm{d}V = \int_{\mathcal{B}}\boldsymbol{N}_{\boldsymbol{u}}^T\rho\boldsymbol{g}\mathrm{d}V + \int_{\Gamma_t}\boldsymbol{N}_{\boldsymbol{u}}^T\bar{t}\mathrm{d}A, \tag{47}$$

$$\begin{aligned}&\int_{\mathcal{B}}\boldsymbol{N}_w^T S_r\boldsymbol{\nabla}\cdot\Delta\boldsymbol{u}\mathrm{d}V + \int_{\mathcal{B}}\boldsymbol{N}_w^T\phi\frac{\partial S_r}{\partial s}\Delta s\mathrm{d}V - \Delta t\int_{\mathcal{B}}\boldsymbol{E}_w^T\bar{\boldsymbol{v}}^w\mathrm{d}V\\ &+\int_{\mathcal{B}}\frac{\tau}{2G}\tilde{\Pi}\boldsymbol{N}_w^T\tilde{\Pi}\Delta p_w\mathrm{d}V = \Delta t\int_{q_w}\boldsymbol{N}_w^T\bar{q}_w\mathrm{d}A,\end{aligned} \tag{48}$$

$$\begin{aligned}&\int_{\mathcal{B}}\boldsymbol{N}_a^T(1-S_r)\boldsymbol{\nabla}\cdot\Delta\boldsymbol{u}\mathrm{d}V - \int_{\mathcal{B}}\boldsymbol{N}_a^T\phi\frac{\partial S_r}{\partial s}\Delta s\mathrm{d}V + \int_{\mathcal{B}}\boldsymbol{N}_a^T\frac{\phi(1-S_r)}{K_a}\Delta p_a\mathrm{d}V\\ &-\Delta t\int_{\mathcal{B}}\boldsymbol{E}_a^T\bar{\boldsymbol{v}}^a\mathrm{d}V + \int_{\mathcal{B}}\frac{\tau}{2G}\tilde{\Pi}\boldsymbol{N}_a^T\tilde{\Pi}\Delta p_a\mathrm{d}V = \Delta t\int_{q_a}\boldsymbol{N}_a^T\bar{q}_a\mathrm{d}A,\end{aligned} \tag{49}$$

where $\Delta s = \Delta p_a - \Delta p_w$ and T is the transpose operator. Accordingly, we can express $\delta\mathscr{G}$, $\delta\mathscr{M}_w$, and $\delta\mathscr{M}_a$ for the kth iteration at time step $n+1$ as follows:

$$\delta \mathscr{G} = \boldsymbol{K}_{uu}\delta \boldsymbol{u} + \boldsymbol{K}_{uw}\delta \boldsymbol{p}_w + \boldsymbol{K}_{ua}\delta \boldsymbol{p}_a, \tag{50}$$

$$\delta \mathscr{M}_w = \boldsymbol{K}_{wu}\delta \boldsymbol{u} + \left(\boldsymbol{K}^1_{ww} + \Delta t\boldsymbol{K}^2_{ww} + \boldsymbol{K}^3_{ww}\right)\delta \boldsymbol{p}_w + \left(\boldsymbol{K}^1_{wa} + \Delta t\boldsymbol{K}^2_{wa}\right)\delta \boldsymbol{p}_a, \tag{51}$$

$$\delta \mathscr{M}_a = \boldsymbol{K}_{au}\delta \boldsymbol{u} + (\boldsymbol{K}^1_{aw} + \Delta t\boldsymbol{K}^2_{aw})\delta \boldsymbol{p}_w + \left(\boldsymbol{K}^1_{aa} + \Delta t\boldsymbol{K}^2_{aa} + \boldsymbol{K}^3_{aa}\right)\delta \boldsymbol{p}_a. \tag{52}$$

From Equations 50, 51, and 52, we can express the global tangent operator as

$$\boldsymbol{\mathcal{K}} = \begin{bmatrix} \boldsymbol{K}_{uu} & \boldsymbol{K}_{uw} & \boldsymbol{K}_{ua} \\ \boldsymbol{K}_{wu} & \boldsymbol{K}^1_{ww} + \Delta t\boldsymbol{K}^2_{ww} + \boldsymbol{K}^3_{ww} & \boldsymbol{K}^1_{wa} + \Delta t\boldsymbol{K}^2_{wa} \\ \boldsymbol{K}_{au} & \boldsymbol{K}^1_{aw} + \Delta t\boldsymbol{K}^2_{aw} & \boldsymbol{K}^1_{aa} + \Delta t\boldsymbol{K}^2_{aa} + \boldsymbol{K}^3_{aa} \end{bmatrix}. \tag{53}$$

Here, the expressions for submatrices in Equation 53 are as follows:

$$\boldsymbol{K}_{uu} = \int_{\mathcal{B}} \boldsymbol{B}^T : \frac{\partial \boldsymbol{\sigma}'}{\partial \boldsymbol{\nabla}^s \boldsymbol{u}} : \boldsymbol{B}\mathrm{d}V, \tag{54}$$

$$\boldsymbol{K}_{uw} = -\int_{\mathcal{B}} \boldsymbol{B}^T : \frac{\partial \boldsymbol{\sigma}'}{\partial s}\boldsymbol{N}_w\mathrm{d}V - \int_{\mathcal{B}} \boldsymbol{b}^T\overline{S_r}\boldsymbol{N}_w\mathrm{d}V, \tag{55}$$

$$\boldsymbol{K}_{ua} = \int_{\mathcal{B}} \boldsymbol{B}^T : \frac{\partial \boldsymbol{\sigma}'}{\partial s}\boldsymbol{N}_a\mathrm{d}V + \int_{\mathcal{B}} \boldsymbol{b}^T(\overline{S_r} - 1)\boldsymbol{N}_a\mathrm{d}V, \tag{56}$$

$$\boldsymbol{K}_{wu} = \int_{\mathcal{B}} \boldsymbol{N}_w^T S_r \boldsymbol{b}\mathrm{d}V, \tag{57}$$

$$\boldsymbol{K}^1_{ww} = -\int_{\mathcal{B}} \boldsymbol{N}_w^T\tilde{\phi}\frac{\partial S_r}{\partial s}\boldsymbol{N}_w\mathrm{d}V, \tag{58}$$

$$\boldsymbol{K}^2_{ww} = \int_{\mathcal{B}} \boldsymbol{E}_w^T(k_{rw}\boldsymbol{k}_w)\boldsymbol{E}\mathrm{d}V - \int_{\mathcal{B}} \boldsymbol{E}_w^T\boldsymbol{k}_w(\boldsymbol{\nabla} p_w + \rho_w\boldsymbol{g})\frac{\partial k_{rw}}{\partial s}\boldsymbol{N}_w\mathrm{d}V, \tag{59}$$

$$\boldsymbol{K}^3_{ww} = \int_{\mathcal{B}} \frac{\tau}{2G}\tilde{\Pi}\boldsymbol{N}_w^T\tilde{\Pi}\boldsymbol{N}_w\mathrm{d}V, \tag{60}$$

$$\boldsymbol{K}^1_{wa} = \int_{\mathcal{B}} \boldsymbol{N}_w^T\tilde{\phi}\frac{\partial S_r}{\partial s}\boldsymbol{N}_a\mathrm{d}V, \tag{61}$$

$$\boldsymbol{K}^2_{wa} = \int_{\mathcal{B}} \boldsymbol{E}_w^T\boldsymbol{k}_w(\boldsymbol{\nabla} p_w + \rho_w\boldsymbol{g})\frac{\partial k_{rw}}{\partial s}\boldsymbol{N}_a\mathrm{d}V, \tag{62}$$

$$\boldsymbol{K}_{au} = \int_{\mathcal{B}} \boldsymbol{N}_a^T(1 - S_r)\boldsymbol{b}\mathrm{d}V, \tag{63}$$

$$\boldsymbol{K}^1_{aw} = \int_{\mathcal{B}} \boldsymbol{N}_a^T\left(\tilde{\phi} + \frac{\phi}{K_a}\Delta p_a\right)\frac{\partial S_r}{\partial s}\boldsymbol{N}_w\mathrm{d}V, \tag{64}$$

$$\boldsymbol{K}^2_{aw} = -\int_{\mathcal{B}} \boldsymbol{E}_a^T\boldsymbol{k}_a(\boldsymbol{\nabla} p_a + \rho_a\boldsymbol{g})\frac{\partial k_{ra}}{\partial s}\boldsymbol{N}_w\mathrm{d}V, \tag{65}$$

$$\boldsymbol{K}^1_{aa} = \int_{\mathcal{B}} \boldsymbol{N}_a^T\left[\frac{\phi(1 - S_r)}{K_a} - \left(\tilde{\phi} + \frac{\phi}{K_a}\Delta p_a\right)\frac{\partial S_r}{\partial s}\right]\boldsymbol{N}_a\mathrm{d}V, \tag{66}$$

$$\boldsymbol{K}^2_{aa} = \int_{\mathcal{B}} \boldsymbol{E}_a^T(k_{ra}\boldsymbol{k}_a)\boldsymbol{E}_a\mathrm{d}V + \int_{\mathcal{B}} \boldsymbol{E}_a^T\boldsymbol{k}_a(\boldsymbol{\nabla} p_a + \rho_a\boldsymbol{g})\frac{\partial k_{ra}}{\partial s}\boldsymbol{N}_a\mathrm{d}V, \tag{67}$$

$$\boldsymbol{K}^3_{aa} = \int_{\mathcal{B}} \frac{\tau}{2G}\tilde{\Pi}\boldsymbol{N}_a^T\tilde{\Pi}\boldsymbol{N}_a\mathrm{d}V. \tag{68}$$

3 | CONSTITUTIVE LAWS

The computational model above is general because we do not define any constitutive model for the solid skeleton and a soil-water characteristic model for the relationship between suction and water content (eg, the degree of water saturation). To close the numerical model, we briefly introduce an elastoplastic constitutive model for the solid skeleton and a soil-water characteristic curve. For the constitutive model and the soil-water retention model, the difference from the previous formulations (eg, Borja et al[8]) is that in this article pore air pressure is explicitly considered in both models.

3.1 | The elastoplastic model for the solid skeleton

The elastoplastic constitutive model for the solid phase is formulated based on an additive decomposition of the total strain of the solid phase in line with the infinitesimal strain theory.

$$\boldsymbol{\epsilon} = \boldsymbol{\epsilon}^e + \boldsymbol{\epsilon}^p, \tag{69}$$

where $\boldsymbol{\epsilon}$ is the total strain tensor, $\boldsymbol{\epsilon}^e$ and $\boldsymbol{\epsilon}^p$ are the elastic strain tensor and plastic strain tensor, respectively. The elastic deformation of the solid phase is determined from a stored energy function $\Psi = \Psi(\boldsymbol{\epsilon}^e)$.[34,77] The effective Cauchy stress tensor is then obtained from the hyperelastic constitutive equation,

$$\boldsymbol{\sigma}' = \frac{\partial \Psi}{\partial \boldsymbol{\epsilon}^e}. \tag{70}$$

To express the yield function via the 3 stress invariants of the effective stress tensor $\boldsymbol{\sigma}'$, we define the mean effective stress p, the deviatoric stress q, and Lode's angle θ as

$$p = \frac{1}{3}\mathrm{tr}(\boldsymbol{\sigma}'), \quad q = \sqrt{\frac{3}{2}}\|\boldsymbol{s}\|, \quad \frac{1}{\sqrt{6}}\cos(3\theta) = \frac{\mathrm{tr}(\boldsymbol{s}^3)}{\chi^3}, \tag{71}$$

where $\boldsymbol{s} = \boldsymbol{\sigma}' - p\mathbf{1}$ and $\chi^2 = \mathrm{tr}(\boldsymbol{s}^2)$. Then we define the yield surface as a function of effective stress, suction stress and degree of saturation S_r,

$$F = \zeta q + p\eta \leqslant 0, \tag{72}$$

where $\zeta = \zeta(\rho, \theta)$ with ρ as a scaling function determined by the ellipticity of yield surface on the π plane, and η is the maximum stress ratio that reads,

$$\eta = (M/N)\left[1 - (1-N)(p/\bar{p}_i)^{N/(1-N)}\right] \text{ and } \bar{p}_i = (1-N)^{(N-1)/N}\bar{p}_c \text{ for } N > 0, \tag{73}$$

where M is the slope of the critical state line, N defines the shape of the yield function, $\bar{p}_i$ is an intermediate plastic variable,[78-80] $\bar{p}_c$ is the effective apparent preconsolidation pressure, and e is the natural number. The plastic internal variable $-\bar{p}_c$ has the physical significance of being the distance from the origin of the stress space to the 'nose' of the yield surface on the compression cap. To describe the influence of the suction and degree of saturation on the yield surface, we use the notion of a bonding variable ξ[7,34,81] that reads

$$\xi = f(s)(1 - S_r), \quad f(s) = 1 + \frac{s/p_{\mathrm{atm}}}{10.7 + 2.4(s/p_{\mathrm{atm}})}, \tag{74}$$

TABLE 1 Material parameters for the constitutive model of the solid phase[8,78,79]

Symbol	Value	Parameter
$\tilde{\kappa}$	0.03	Compressibility
p_0	−0.1 MPa	Reference pressure
μ_0	20 MPa	Shear modulus
M	1.2	Critical state parameter
$\tilde{\lambda}$	0.11	Compressilibity parameter
N	0.4	Yield surface parameter
h	280	Hardening modulus
ν_{c0}	1.80	Reference specific volume
ρ	7/9	Ellipticity
α	−3.5	Limit dilatancy parameter

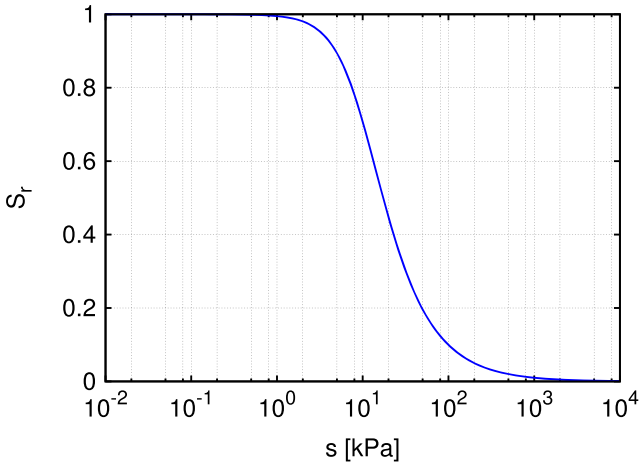

FIGURE 1 A soil water characteristic curve

TABLE 2 Material parameters for the flow of pore water and pore air

Symbol	Value	Parameter
k_w	0.5×10^{-6} m/s	Saturated permeability of pore water
k_a	0.5×10^{-8} m/s	Saturated permeability of pore air
S_1	0.0	Soil-water retention model parameter
S_2	1.0	Soil-water retention model parameter
n	2.0	Soil-water retention model parameter
s_a	10.0 kPa	Air entry pressure
c_1	0.185 kPa	Parameter of ξ^{81}
c_2	1.49	Parameter of ξ^{81}
p_{atm}	101.3 kPa	Atmospheric pressure

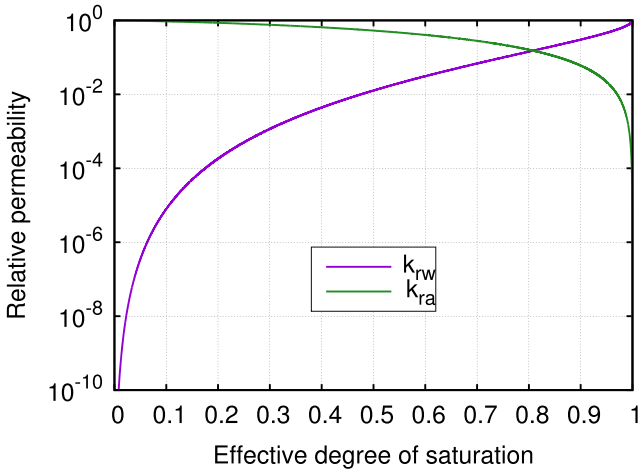

FIGURE 2 Relative permeabilities of pore water and pore air

where $p_{\text{atm}} = 101.3\,\text{kPa}$ is the atmosphere pressure. The equivalent preconsolidation pressure $\bar{p}_c$ is then given by

$$\bar{p}_c = -\exp[a(\xi)](-p_c)^{b(\xi)}, \tag{75}$$

where $c(\xi)$, $a(\xi)$ and $b(\xi)$ are functions of ξ.[34,81]

The plastic flow is assumed as the associative, that is, the plastic potential function is the same as Equation 72. Finally, the return mapping algorithm with the spectral decomposition in the principal strain space is used to implement this model at the

material point level (refer to Borja et al[8] for details). As a byproduct, the material subroutine also provides the consistent tangent operator at the material point level. Table 1 shows input parameters for the solid phase under the fully saturated condition.

3.2 | Soil-water characteristic curve and relative permeabilities

Soil water characteristic curve (or soil water retention law) is a fundamental law in modeling deformation and fluid flow in unsaturated soils[4,82] that builds a relationship between the water content and water potential. In this article, we use the van Genuchten equation[48] to describe the soil-water characteristic curve as follows:

$$S_r = S_1 + (S_2 - S_1)\left[1 + \left(\frac{s}{s_a}\right)^n\right]^{-m}, \tag{76}$$

where s_a is the air entry value and S_1, S_2, n, and $m = (n-1)/n$ are fitting parameters. Let the effective degree of saturation[48] α be

$$\alpha = \frac{S_r - S_1}{S_2 - S_1}. \tag{77}$$

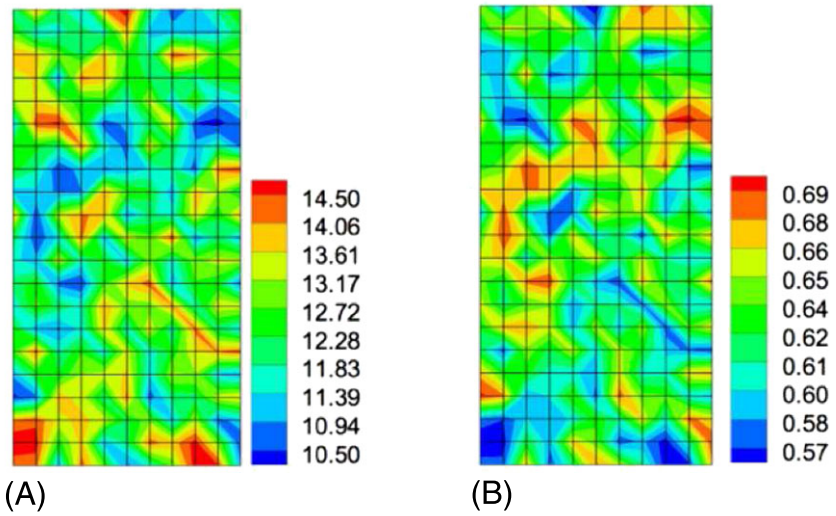

FIGURE 3 Contours of A, initial suction (unit: kPa) assuming zero initial air pressure and B, initial degree of saturation superimposed of sample #1 on the undeformed mesh

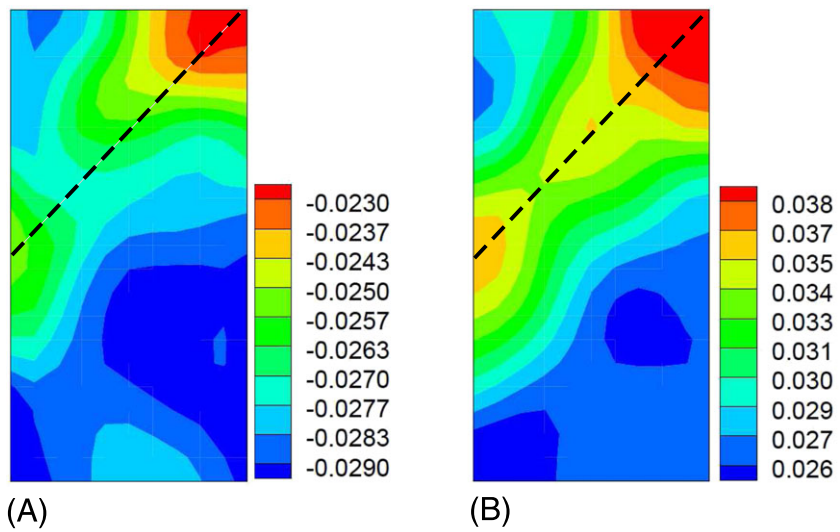

FIGURE 4 Contours of A, volumetric strain and B, shear strain of sample #1 at a nominal axial strain of 5%. Note: The dashed black line delineates the localized deformation zone and its potential propagation path

Then, the relative permeabilities of the water phase and the air phase are assumed as[1,48]

$$k_{rw} = \alpha^{1/2}\left[1 - \left(1 - \alpha^{1/m}\right)^{m}\right]^{2}, \tag{78}$$

$$k_{ra} = (1 - \alpha)^{1/2}\left(1 - \alpha^{1/m}\right)^{2m}, \tag{79}$$

where m is the same material parameter in Equation 76. Figure 1 shows a water retention curve based on the parameters in Table 2. Figure 2 presents the relative permeabilities of pore water and pore air, respectively.

4 | NUMERICAL SIMULATIONS

In this section, we conduct the numerical simulation of unsaturated soil samples under the plane strain condition via the three-phase computational framework. We first run simulations of 2 samples with an initial heterogeneous state either in suction or dry density. We investigate the evolution of pore air pressure across the localized zone and its potential impact on the

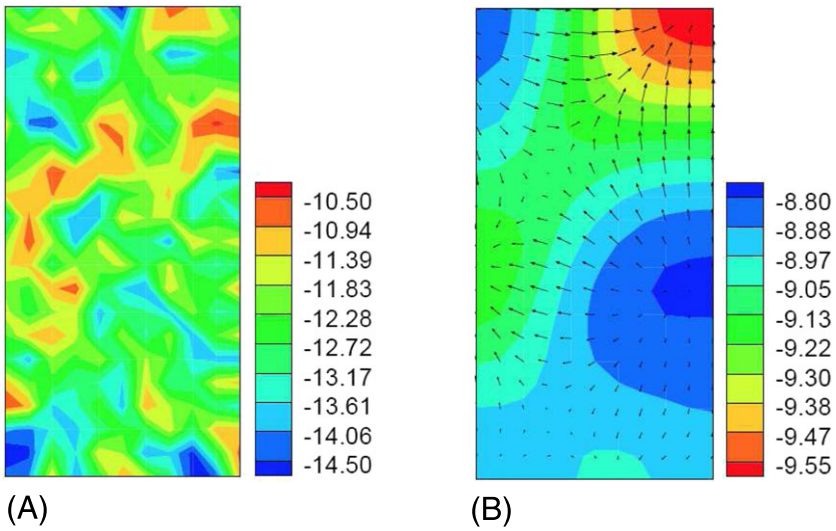

FIGURE 5 Contours of A, initial pore water pressure (unit: kPa) and B, pore water pressure (unit: kPa) of sample #1 at a nominal axial strain of 5% (arrows represent water flow direction) superimposed on the undeformed sample domain

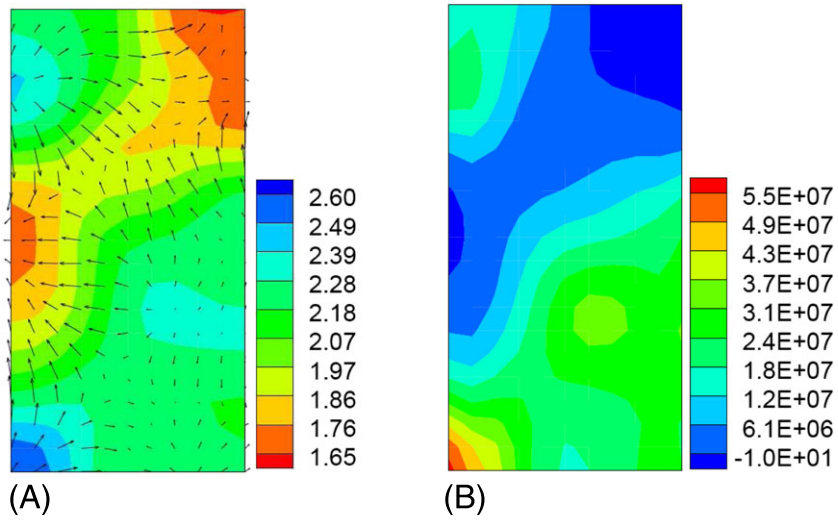

FIGURE 6 Contours of pore air pressure (unit: kPa, and arrows represent air flow direction) (A), and the drained localization function[8] (B) in sample #1 at a nominal axial strain of 5% superimposed on the undeformed sample domain

inception of strain localization. Secondly, we compare the numerical results via the three-phase model and the two-phase formulation assuming passive air pressure, respectively. Finally, we conduct the simulations of an unsaturated soil sample with both coarse and finer meshes to study the mesh sensitivity of the numerical results.

All samples are 5 cm wide and 10 cm high. Except for the mesh sensitivity analysis, the samples are discretized by 200 equal stabilized trilinear quadrilateral elements. The stabilized low-order (trilinear) quadrilateral elements[8,49,71,83] are used to suppress spurious pore pressure oscillations in the incompressible and nearly incompressible regimes. For the mechanical boundary conditions, the bottom of each rectangular specimen is fixed in the vertical direction except that the left corner is pinned for the stability. The lateral sides of each sample are prescribed with constant confining pressure, 100 kPa. A vertical displacement is assigned on the top of the specimen as a loading protocol. For the fluid flow boundary conditions, zero flux of pore water and pore air are prescribed on all boundaries. For all samples, the initial pore air pressure is assumed as passive atmospheric pressure. However, the three-phase framework will track the evolution of pore air pressure in the coupled processes of solid deformation and fluid flow.

4.1 | Compression of heterogeneous samples under the plane strain condition

In this part, we run numerical simulations of 2 unsaturated soil samples under the plane strain condition. A heterogeneous initial state either in suction or density is prescribed in the sample as described in the succeeding text. To simulate a local drained condition, we prescribe a displacement loading rate 0.001 mm/s on the top of each sample that may be treated as a quasi-static

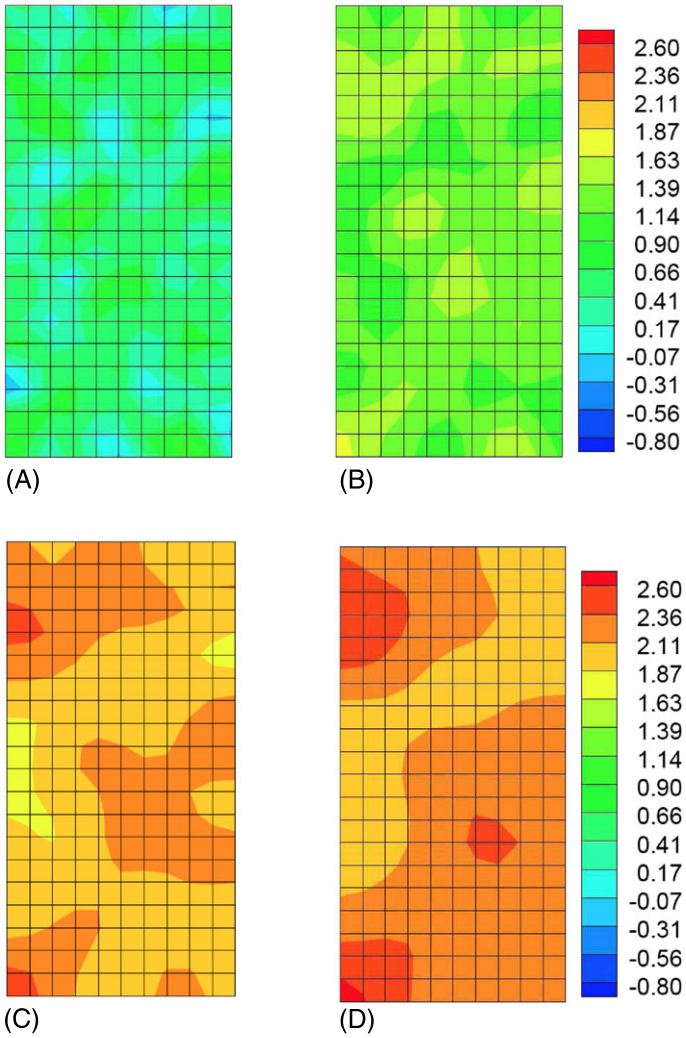

FIGURE 7 Snapshots of the contour of pore air pressure (unit: kPa) at the load time step A, 50, B, 150, C, 350, and D, 450, superimposed on the undeformed mesh

loading condition (refer to Song and Borja[7] for detailed discussions). The temporal increment for each load step is 1 second. The simulations are terminated when a developed localized deformation zone forms in the sample.

For Case #1, we run simulations of a sample (sample #1) with an initial heterogeneity in the form of suction. For the simplicity, the initial random suction field is generated by the standard random function on MATLAB. We refer the reader to Meftah et al[14] and others[84,85] for more complex methods of generating random data for modeling the heterogeneity effect of geomaterials. There are 231 sample suction points corresponding to 231 nodes in the problem domain. That is, the suction is assigned on the global nodal point. The range of the initial random suction is [10.02, 14.98] (unit: kPa) with a mean value 12.49 and a standard deviation 1.45. The initial degree of saturation of each element node in the sample is computed from Equation 76. Note here we assume that the degree of saturation of each element node is independent of the volumetric strain of the same material point for the formulation based on the small strain theory (refer to Song and Borja[7] for a strain-dependent soil-water retention law). Figure 3A,B shows the contours of initial suction and initial degree of saturation superimposed on the undeformed mesh of the problem domain, respectively. Figure 3A represents a heterogeneous state of suction in the sample. Therefore, under the homogeneous boundary condition and a loading protocol favoring homogeneous deformation, we can expect that the localized deformation in the sample would be triggered by the initial heterogeneity in suction.

To demonstrate the localized deformation, we report the numerical results at a nominal axial strain of 5%. Figure 4 portrays the contours of the volumetric strain and shear strain in the sample at the same nominal axial strain of 5%. Firstly, from Figure 4A,

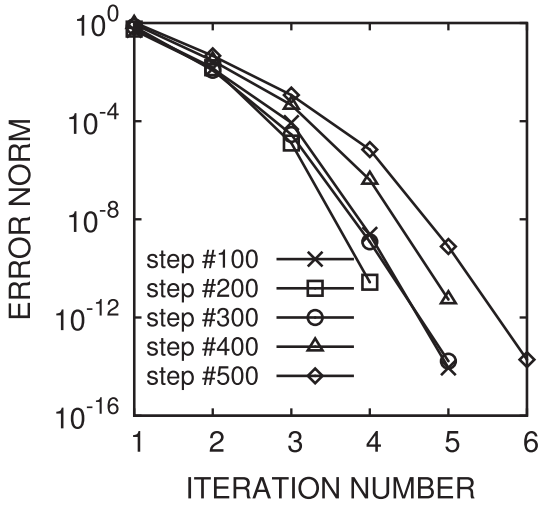

FIGURE 8 Typical global convergence of Newton iterations for sample #1

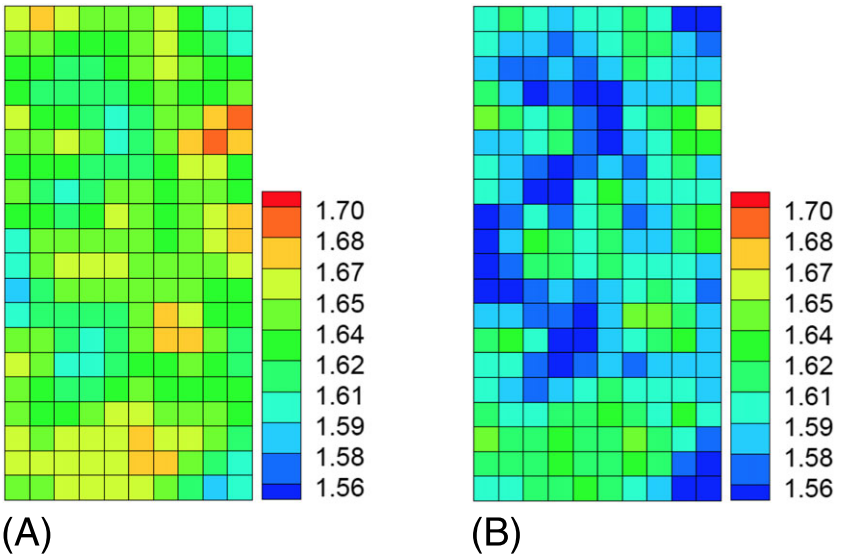

FIGURE 9 Contours of the initial specific volume (A) and the final specific volume (B) of sample #2 at a nominal axial strain of 5%

we obviously observe that the a localized deformation zone forms in the sample from the right upper corner to the middle of the left side of the sample. Furthermore, Figure 4A illustrates that the volumetric strain in the localized deformation zone is smaller than that outside the localized zone. However, the deviatoric (or shear) strain in the localized zone as shown in Figure 4B is much greater than that outside the localized deformation zone. As in Borja,[86] we may conclude the localized deformation in the sample is a compaction shear band.

Next, we present the results of pore water pressure and pore air pressure. To demonstrate the evolution of pore water pressure and pore air pressure, we compare their final states with their initial states, respectively. Figure 5A,B presents the contours of initial pore water pressure and pore water pressure at a nominal axial strain of 5.0%. From Figure 5, we observe that the distribution of pore water pressure becomes relatively uniform although we can observe a localized zone in the sample. The water flows into the localized zone as shown by the flux arrows in Figure 5B. This result may be explained by the fact that the pore water pressure is smaller (more negative) inside the localized zone than that outside the localized zone. Figure 6A,B shows the contour of the pore air pressure and the drained localized function[34] at a nominal axial strain of 5.0%, respectively. From Figure 6A, we observe that pore air pressure is nonzero in the sample under the global undrained condition. Furthermore,

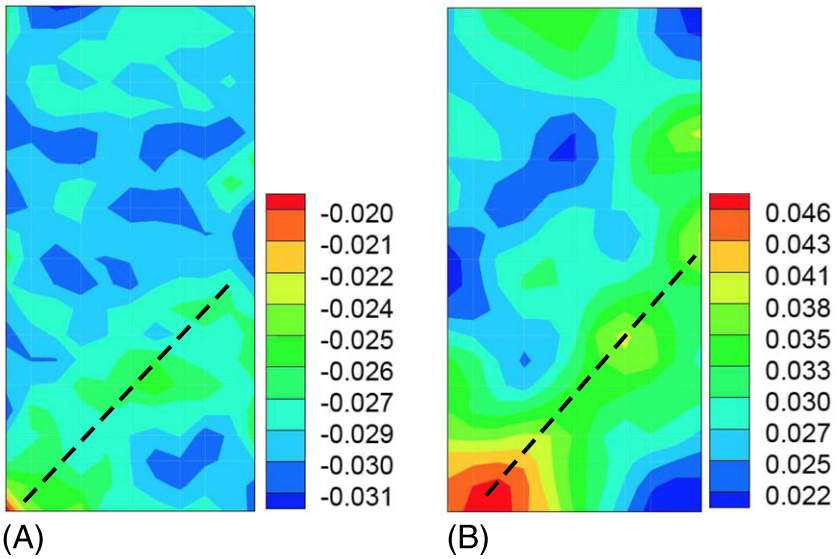

FIGURE 10 Contours of (A) volumetric strain and (B) shear strain in sample #2 at a nominal axial strain of 5.0%. Note: The dashed black line delineates the localized deformation zone and its potential propagation path

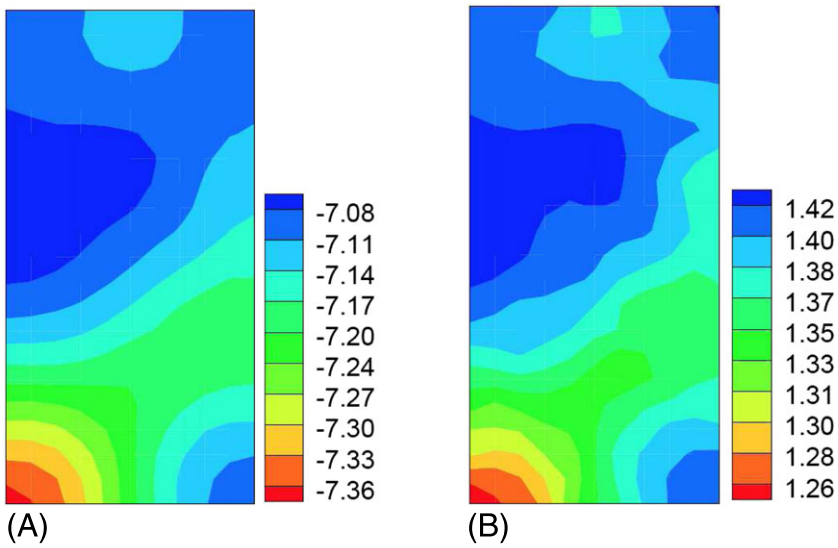

FIGURE 11 Contours of pore water pressure (A) and pore air pressure (B) in sample #2 at a nominal axial strain of 5%. Note: The unit in the contour legend is kPa

Figure 6A demonstrates that pore air pressure in the localized zone have a relatively smaller value than that outside the localized zone in the sample. This fact is also corroborated by the phenomenon that the pore air flux into the localized zone as shown by the flux arrows in Figure 6A. Figure 6A,B shows that the localized zone of pore air pressure is consistent with the localized deformation zone in the sample as demonstrated by the similarity of the contour patterns in both figures. To study the evolution of pore air pressure in the sample during the loading process, we present the snapshots of the contour of pore air pressure at 4 load steps in Figure 7. These 4 snapshots of the contour of pore air pressure share the same contour legend. The pore air pressure in these snapshots is nonzero in the sample, as it may be expected for the simulation under a global undrained condition of pore water and pore air. Also, the distribution of pore air pressure in the sample becomes heterogeneous from its initial homogeneous state (ie, the atmospheric pressure). Moreover, Figure 7A shows that pore air pressure at some nodal points is negative. Clearly, those observed phenomena cannot be captured by a two-phase computational framework assuming passive air pressure. Note that the absolute pore air pressure equals to the summation between the value of the contour and the atmospheric pressure.

Finally, Figure 8 illustrates typical global convergence profiles of Newton iterations. Figure 8 demonstrates that the simulations have a quasi-quadratic convergence rate for sample #1 that is a typical characteristic of Newton's method. We achieve this optimal convergence rate by implementing a global consistent tangent operator and a local consistent tangent operator from the material subroutine via the classic return mapping algorithm for computational plasticity.[58,86]

For Case #2, we run simulations of an unsaturated soil sample (sample #2) with an initial heterogeneous state in the specific volume and a uniform suction in the sample. The initial state of the specific volume is also generated by the random function on

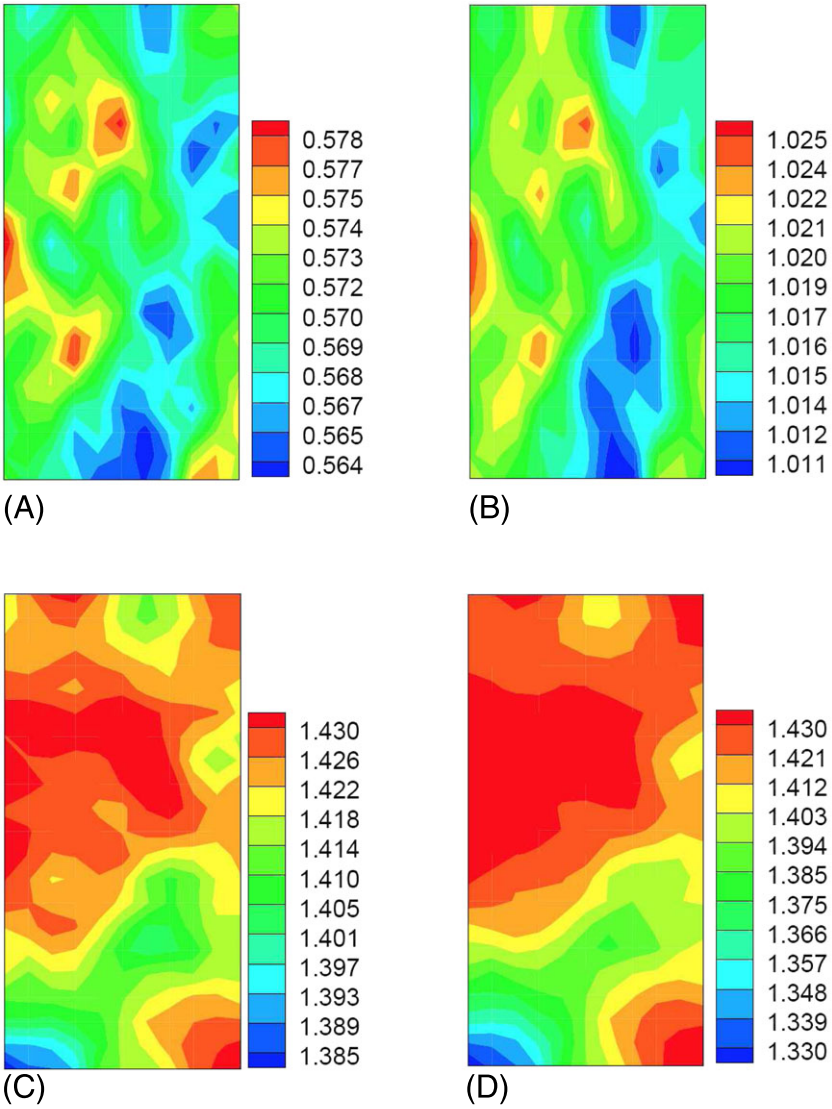

FIGURE 12 Snapshots of the contour of pore air pressure (unit: kPa) at load steps of A, 100, B, 200, C, 300, and D, 450

MATLAB. The sample points of the heterogeneity in the specific volume are assigned in the sample by an element-by-element fashion (ie, all Gauss points of the same element have the same specific volume) that is different from the method used for sample #1. Because there are total 200 equal elements in the sample, we only need to generate 200 sample points for the specific volume. That is, each element has a uniform initial specific volume. The initial water pressure in the sample is prescribed as −10 kPa, and pore air pressure is assumed as zero. Figure 9A shows the contour of a realization of initial specific volume in the sample. The range of the specific volume shown in Figure 9A is [1.55, 1.72] with a mean value 1.64 and a standard deviation 0.048. In the numerical model, for all Gauss points in each element, we assume they share the same initial specific volume. To show a relatively developed localized deformation zone in sample #2, we report the numerical results at a nominal axial strain of 5%. Figure 9B shows the contour of the heterogeneous specific volume of the sample superimposed on the undeformed mesh at a nominal axial strain of 5%.

Figure 10 shows the contours of the volumetric strain and shear strain in sample #2 at a nominal axial strain of 5%. From Figure 10A,B, we observe that a compact shear band forms in the sample from the left corner to the upper left side of the sample. Figure 11 shows the contours of pore water pressure and pore air pressure in the sample at a nominal axial strain of 5.0%. From Figure 11A, we observe that pore water pressure inside the localized deformation zone is smaller (negative) than that outside the localized zone. Similarly, pore air pressure within the localized deformation area is smaller than that outside the localized area. To study the evolution of pore air pressure in the loading process, we present the snapshots of the contour

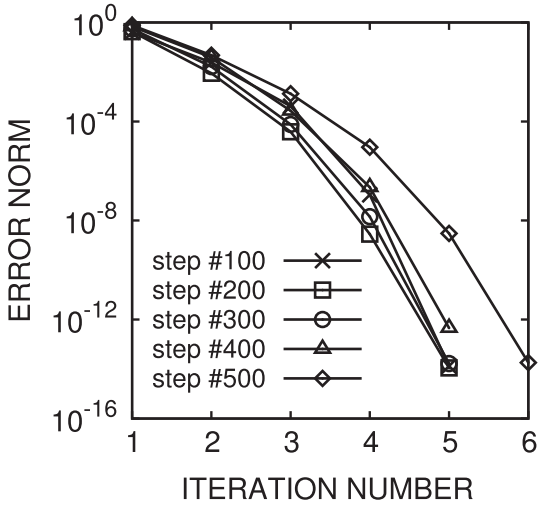

FIGURE 13 Typical global convergence of Newton iteration for sample #2

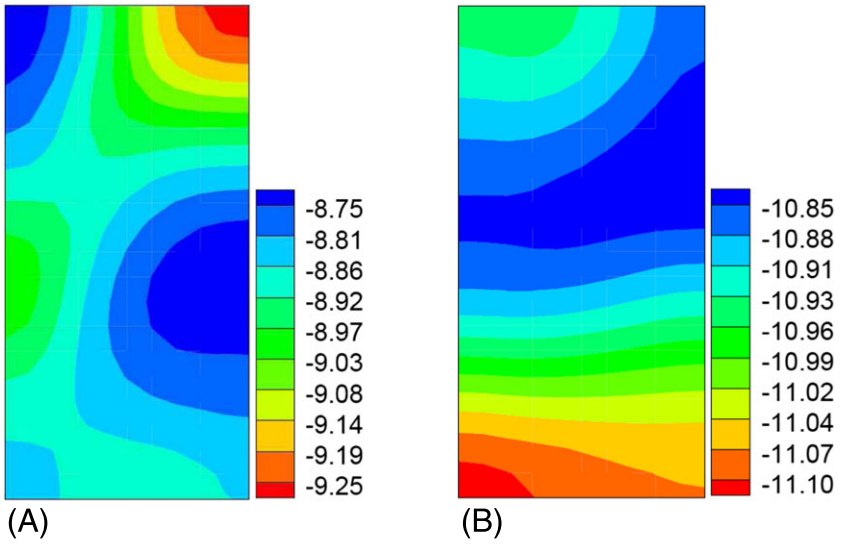

FIGURE 14 Contours of water pressure, A, from three-phase model, B, from the two-phase model assuming passive air pressure at an axial nominal strain of 5% for sample #1

of pore air pressure in sample #2 at 4 loading steps as shown in Figure 12. In Figure 12, we use different contour legends for each contour of pore air pressure to better capture the heterogeneity and evolution of pore air pressure in the sample. Figure 12 clearly demonstrates that pore air pressure is nonuniform in the problem domain through the loading process. At the load step of 300, a banded zone of lower pore air pressure forms from the lower left corner to the upper right side of sample #2. This banded zone is consistent with the localized deformation zone in the sample as shown in Figure 10.

Finally, Figure 13 shows the typical global convergence profiles of Newton's method for sample #2. From Figure 13, we conclude that the optimal convergence rate is obtained for the numerical simulation of sample #2.

4.2 | Comparison with results obtained from the pseudo three-phase formulation

In this part, we compare the numerical results above with that from the two-phase model by assuming passive pore air pressure throughout the sample domain. We rerun the simulation of samples #1 and #2 via the two-phase model (ie, constant atmospheric pressure) under the same initial and boundary conditions and the same loading rate.

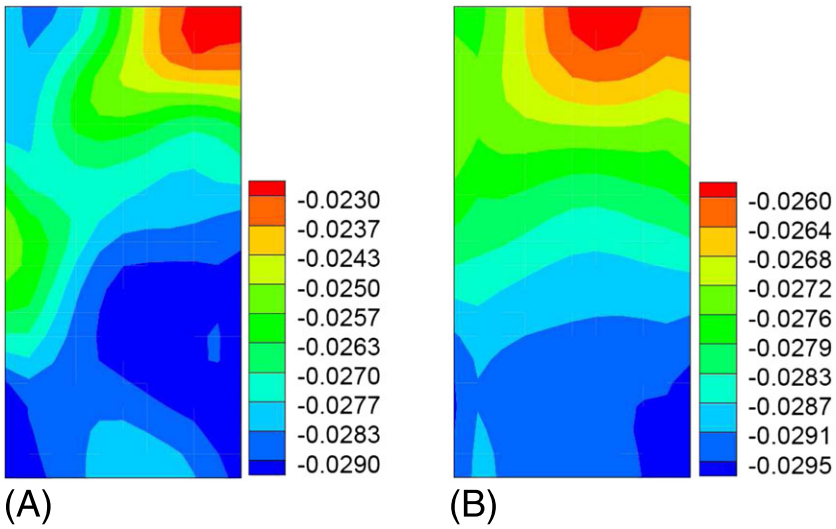

FIGURE 15 Contours of volumeric strain, A, from three-phase model, B, from the two-phase model assuming passive air pressure at an axial nominal strain of 5% for sample #1

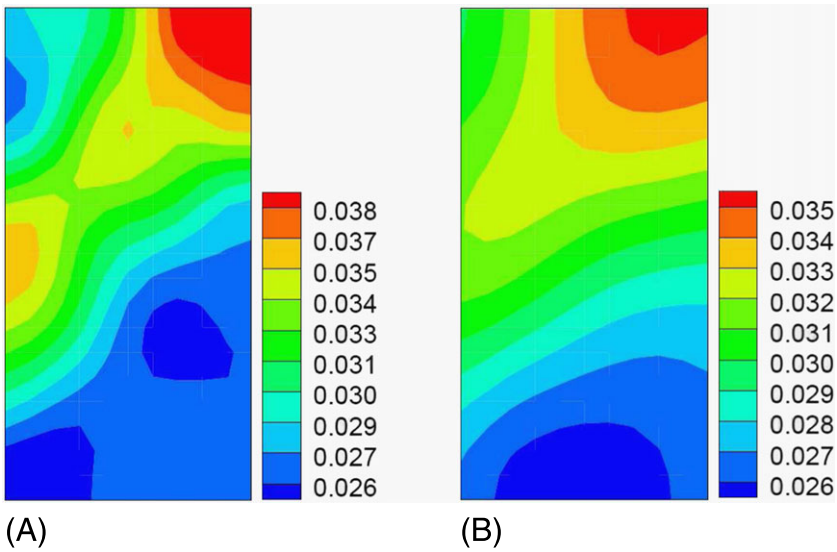

FIGURE 16 Contours of deviatoric strain, A, from three-phase model, B, from the two-phase model assuming passive air pressure at an axial nominal strain of 5%

We first compare the results from both frameworks for sample 1. Figure 14 shows the contours of pore water pressure in the sample from both models at the same nominal axial strain of 5%. We observe from Figure 14 that the absolute value of pore water pressure predicted from the three-phase model is smaller than that from the two-phase model. Furthermore, Figure 14 demonstrates that for sample 1, pore water pressure from the two-phase model is more uniform than the result from the three-phase model. Figure 15 shows the contours of volumetric strain from the simulations via both computational models, respectively, at a nominal axial strain of 5%. From Figure 15, we observe the distribution and the range of the volume strain based on both models are not identical. It turns out the volume strain from the three-phase model is more localized than that from the two-phase model. Figure 16A,B shows the contours of the shear strain in the sample via both frameworks, respectively, at a nominal axial strain of 5%. From Figure 16A,B, we observe both frameworks can simulate the localized deformation sample# under the same initial and boundary conditions. However, the three-phase model predicts a larger shear strain in sample #1 than the two-phase model does.

Next, we present the simulation results of sample #2 from the two-phase model and compare them with the results from the three-phase model. Figure 17A,B shows the contours of pore water pressure from the two-phase model and three-phase model,

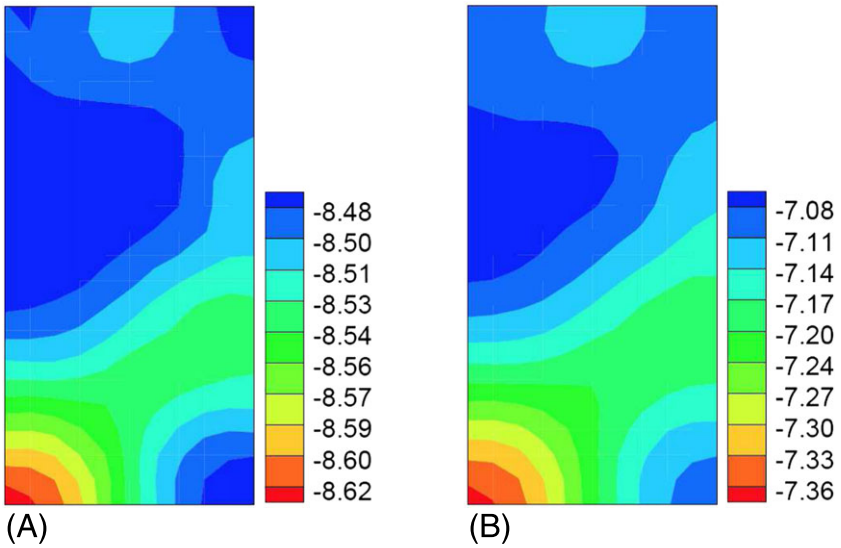

FIGURE 17 Contours of water pressure, A, from two-phase model assuming passive air pressure, B, from the three-phase model at an axial nominal strain of 5%

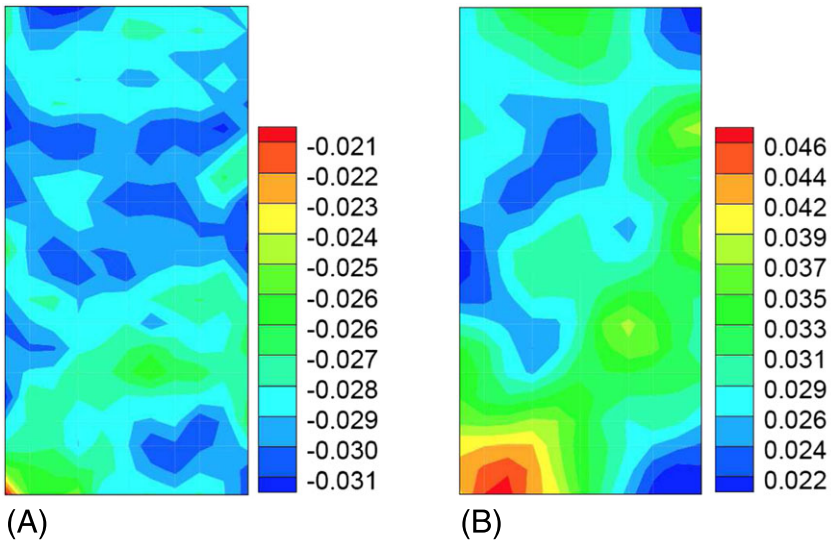

FIGURE 18 Contours of A, volumetric strain and B, shear strain from the two-phase model assuming passive air pressure at an axial nominal strain of 5%

respectively, at the same nominal axial strain 5%. From Figure 17A,B, we observe that the contour of pore water pressure from both models shares a similar pattern. However, the absolute value of pore water pressure from the three-phase model is smaller than that predicted from the two-phase model. Refer to the pore air pressure in sample #2 at the same axial strain as shown in Figure 11B, the smaller absolute value of negative pore water pressure from the three-phase model can be explained by the fact that the suction is partially transferred to the positive pore air pressure in the three-phase model. However, the two-phase model assuming the passive pore air pressure cannot capture the evolution of pore pressure in the coupled multiphysical processes. Figure 18A,B presents the contours of volumetric strain and shear strain in sample #2 at a nominal axial strain of 5%. From Figure 18, we observe that both volume strain and deviatoric strain show similar localized patterns from the left corner to the middle of the right side of the sample. The result from the two-phase model is consistent with that predicted from the three-phase model as illustrated in Figure 10. However, the two-phase model cannot simulate the evolution of pore air pressure in the sample.

In summary, by comparing the numerical results obtained by both formulations, we demonstrate that the triphasic formulation can capture more physical information such as the heterogeneity of pore air pressure and the air flow in the pore space than the equivalent two-phase formulation. Furthermore, the variation of pore air pressure captured by the three-phase model may be important for modeling localized deformation triggered by initial heterogeneous suction (eg, sample #1).

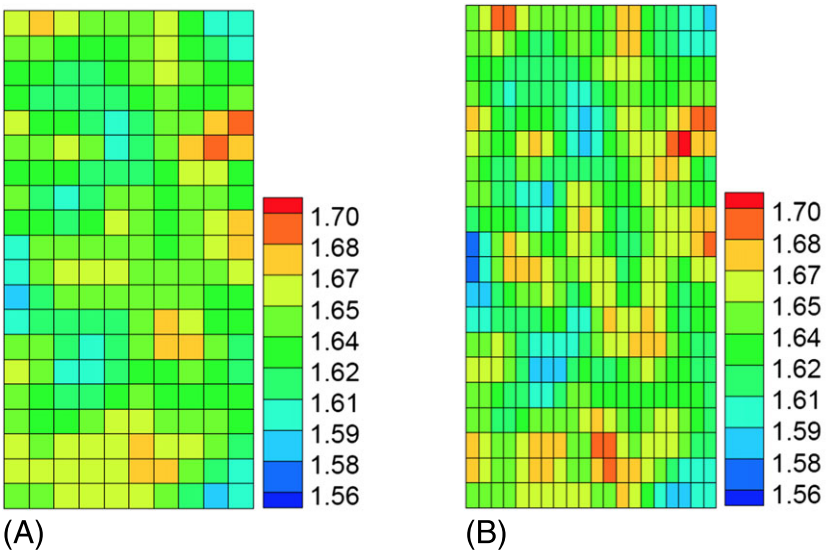

FIGURE 19 Contours of the initial specific volume in the A, coarse mesh and in the B, finer mesh

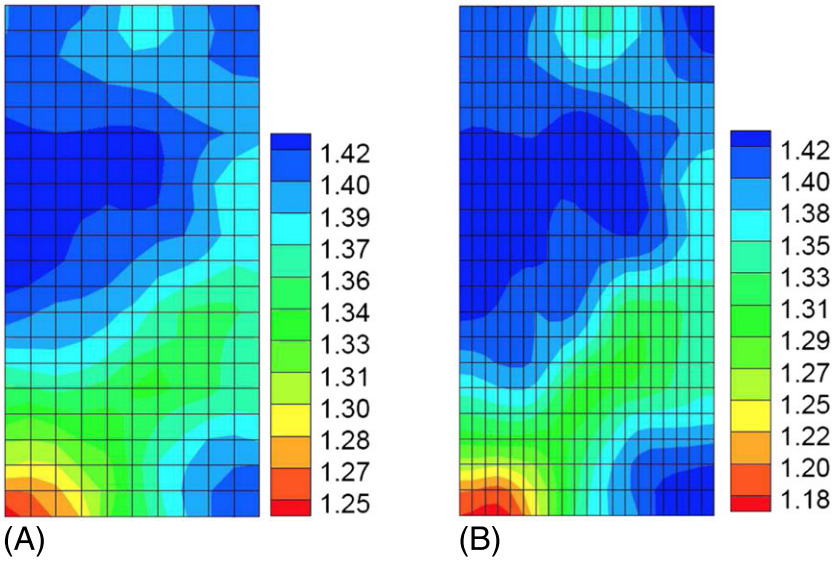

FIGURE 20 Contours of pore air pressure from the simulations via the A, coarse mesh and via the B, finer mesh at an axial nominal strain of 5%

4.3 | Mesh sensitivity analysis

The numerical simulations presented in this article is based on the mixed finite element method. The finite element method has pathological issues in simulating localized deformation in materials as discussed in De Borst et al.[22] To test the mesh sensitivity of the numerical results presented here, we conduct simulations of sample #2 with a finer mesh as shown in Figure 19A. All simulations are conducted with the three-phase model. Figure 19A,B shows that the contours of initial specific volume superimposed on the coarse mesh and finer mesh, respectively. The finer mesh is generated from the coarse mesh by vertically dividing each element in the coarse mesh into 2 equal elements. Both equal elements are assigned with the same initial specific volume as the corresponding element in the coarse mesh has.

Figure 20A,B shows the contours of pore air pressure from the simulations via both meshes, respectively. From Figure 20A,B, we do not observe a significant difference between the results from both meshes although the results from the finer mesh have a higher resolution. Figure 21A,B portrays the contours of volumetric strain in sample #2 from the simulations via the coarse mesh and finer mesh, respectively. From Figure 21, we can identify subtle difference between both numerical results. For example, the contour of the volumetric strain from the simulation via the finer mesh shows a narrower localized zone from the left bottom corner to the middle of the right side of the sample. In this zone, the volumetric strain is smaller than that outside the localized zone. However, the contour of the volumetric strain from the simulation via the coarse mesh shows a wider

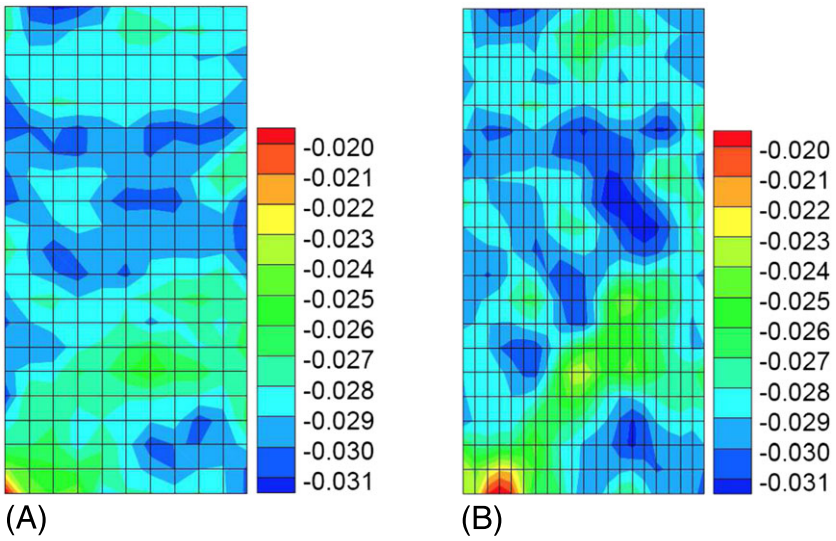

FIGURE 21 Contours of volumetric strain from the simulations via the A, coarse mesh and via the B, finer mesh at an axial nominal strain of 5%

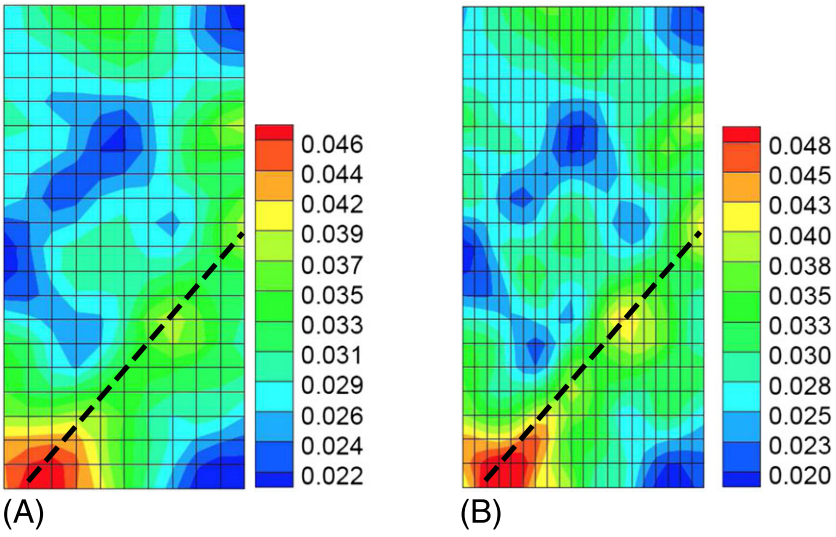

FIGURE 22 Contours of deviatoric strain from the simulations via the A, coarse mesh and via the B, finer mesh at an axial nominal strain of 5%. Note: The dashed black line delineates the localized deformation zone and its potential propagation path

localized zone. This mild contrast shown in Figure 21 demonstrates that the numerical results have a mild sensitivity on the mesh. Figure 22A,B presents the contours of shear strain from the simulations via the coarse and finer meshes, respectively, at a nominal axial strain of 5%. Figure 22 demonstrates that the similar contours of shear strain are obtained from the simulations via both meshes. Figure 23 shows the load curves from the simulations via both meshes. From Figure 23, we observe that both curves are overlapped in the earlier stage of the load process. However, the load curve for the fine mesh shows a mild softening effect on the later stage of the loading process (ie, the axial strain greater than 3.5%). Finally, Figure 24 shows the optimal convergence rates obtained at sample load steps for the simulations with the finer mesh.

4.4 | Remarks on the mild mesh sensitivity

The physical reason behind this observed mild mesh sensitivity may be related to the rate dependent term (ie, generalized Darcy's law) in the mass balance equations of pore water and pore air. An internal length scale that serves as a natural regularization parameter[87] could exist in the mixed finite element formulation for multiphase porous media[39,88] such as the one formulated in this article. However, as discussed in Zhang and Schrefler,[39] this internal length scale may be dependent on the intrinsic permeability of the fluid phase. We refer the reader to the previous studies[39,41,89,90] for further discussions on this subject.

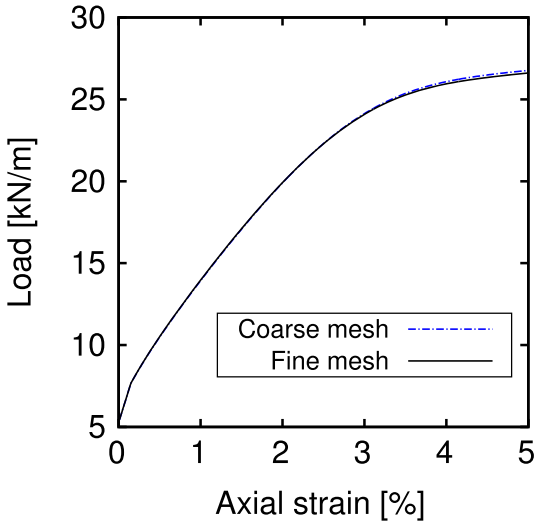

FIGURE 23 Load curves of sample #2 from the simulations via the coarse mesh and the finer mesh, respectively

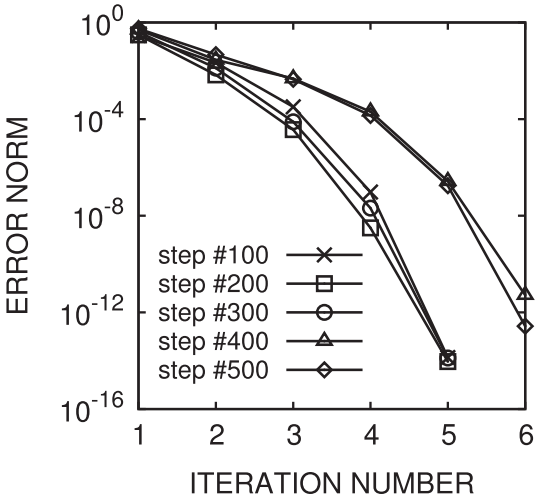

FIGURE 24 Typical global convergence of Newton iteration for the simulations of sample #2 with the finer mesh

5 | CONCLUSION

In this article, we formulate a three-phase computational framework for solid-water-air coupling in unsaturated porous media to investigate strain localization in such a solid-water-air system. To obtain an optimal convergence rate, we derive a global consistent tangent operator that includes a local consistent tangent operator at the material point level. This three-phase model is implemented via stabilized low-order mixed finite elements.Via this three-phase model, we study the evolution of pore air pressure within unsaturated soil samples involving strain localization triggered by the initial material heterogeneity either in density or suction. The pore air pressure in the samples becomes heterogeneous in the loading process under a global undrained condition. We highlight the significance of the pore air phase in computational modeling of strain localization in unsaturated soils. We find that the pore air pressure within the compact shear band formed in the samples is smaller than the pore air pressure outside the localized zone. Numerical results imply that the three-phase model is physically more appropriate to simulate the inception of strain localization in unsaturated soils than the two-phase formulation assuming constant pore air pressure.

ACKNOWLEDGEMENTS

The authors are grateful to 2 anonymous reviewers for their constructive comments. Their expert reviews have helped to improve the paper substantially.

REFERENCES

1. Coussy O. *Poromechanics*: Wiley; Chichester 2004.
2. Fung Y-C. *Biomechanics: Mechanical Properties of Living Tissues*: Springer Science & Business Media; New York1993.
3. Cowin SC, Doty SB. *Tissue Mechanics*: Springer Science & Business Media; New York 2007.
4. Lu N, Likos WJ. *Unsaturated Soil Mechanics*: Wiley; Hoboken, New Jersey 2004.
5. Song X, Idinger G, Borja RI, Wu W. Finite element simulation of strain localization in unsaturated soils. In: Mancuso C., Jommi C., D'Onza F. (eds) *Unsaturated Soils: Research and Applications*: Springer; Berlin Heidelberg 2012:189-195.
6. Song X, Borja RI, Wu W. Triggering a shear band in variably saturated porous materials. In: Hellmich C., Pichler B., Adam D. (eds) Poromechanics v@ Sproceedings of the Fifth Biot Conference on Poromechanics ASCE; Vienna, Austria 2013:367-370.
7. Song X, Borja RI. Mathematical framework for unsaturated flow in the finite deformation range. *Int J Numer Methods Eng*. 2014;97(9):658-682.
8. Borja RI, Song X, Wu W. Critical state plasticity. part vii: triggering a shear band in variably saturated porous media. *Comput Methods Appl Mech Eng*. 2013;261:66-82.
9. Song X. Strain localization in unsaturated porous media. *Ph.D. Thesis*: Stanford University; 2014.
10. Song X. Transient bifurcation condition of partially saturated porous media at finite strain. *Int J Numer Anal Methods Geomech*. 2017; 41(1):135-156.
11. Wheeler SJ. The stress-strain behaviour of soils containing gas bubbles. *Ph.D. Thesis*: University of Oxford; 1986.
12. Pietruszczak S, Pande GN. A description of the undrained response of gas bearing soils. *Numog IV*. 1992;1:169-178.
13. Sanavia L, Pesavento F, Schrefler BA. Finite element analysis of non-isothermal multiphase geomaterials with application to strain localization simulation. *Comput Mech*. 2006;37(4):331-348.
14. Meftah F, Dal Pont S, Schrefler BA. A three-dimensional staggered finite element approach for random parametric modeling of thermo-hygral coupled phenomena in porous media. *Int J Numer Anal Methods Geomech*. 2012;5:574-596.
15. Laloui Lyesse, Klubertanz Georg, Vulliet Laurent. Solid–liquid–air coupling in multiphase porous media. *Int J Numer Anal Methods Geomech*. 2003;27(3):183-206.
16. Ehlers W, Graf T, Ammann M. Deformation and localization analysis of partially saturated soil. *Comput Methods Appl Mech Eng*. 2004;193(27):2885-2910.
17. VARDOULAKIS I, SULEM J. Bifurcation analysis in geomechanics. Blackie Academic & Professional, Bishopbriggs, Glasgow 1995.
18. Borja RI. Bifurcation of elastoplastic solids to shear band mode at finite strain. *Comput Methods Appl Mech Eng*. 2002;191(46):5287-5314.
19. Rudnicki JW, Rice JR. Conditions for the localization of deformation in pressure-sensitive dilatant materials. *J Mech Phys Solids*. 1975;23(6):371-394.
20. Rice J, Rudnicki J. A note on some features of the theory of localization of deformation. *Int J Solids Struct*. 1980;16(7):597-605.
21. Bigoni Davide, Hueckel Tomasz. Uniqueness and localization-i. associative and non-associative elastoplasticity. *Int J Solids Struct*. 1991;28(2):197-213.
22. De Borst R, Sluys LJ, Muhlhaus H-B, Pamin J. Fundamental issues in finite element analyses of localization of deformation. *Eng Comput*. 1993;10(2):99-121.
23. Cervera M, Chiumenti M, de Saracibar CA. Shear band localization via local j 2 continuum damage mechanics. *Comput Methods Appl Mech Eng*. 2004;193(9):849-880.
24. Vardoulakis I. Stability and bifurcation of undrained, plane rectilinear deformations on water-saturated granular soils. *Int J Numer Anal Methods Geomech*. 1985;9(5):399-414.

25. Vardoulakis I. Deformation of water-saturated sand: Ii. effect of pore water flow and shear banding. *Géotechnique*. 1996;46(3):457-472.
26. Finno RJ, Harris WW, Mooney MA, Viggiani G. Strain localization and undrained steady state of sand. *J Geotech Eng*. 1996;122(6):462-473.
27. Andrade JE, Borja RI. Modeling deformation banding in dense and loose fluid-saturated sands. *Finite Elem Anal Des*. 2007;43(5):361-383.
28. Oliver J, Huespe AE, Dias IF. Strain localization, strong discontinuities and material fracture: matches and mismatches. *Comput Methods Appl Mech Eng*. 2012;241:323-336.
29. Benedetti L, Cervera M, Chiumenti M. Stress-accurate mixed fem for soil failure under shallow foundations involving strain localization in plasticity. *Comput Geotech*. 2015;64:32-47.
30. Tjioe M, Borja RI. Pore-scale modeling of deformation and shear band bifurcation in porous crystalline rocks. *Int J Numer Methods Eng*. 108:183-212 2016.
31. Semnani SJ, White JA, Borja RI. Thermoplasticity and strain localization in transversely isotropic materials based on anisotropic critical state plasticity. *Int J Numer Anal Methods Geomech*. 2016;40(18):2423-2449.
32. van den Eijnden A, Bésuelle P, Collin F, Chambon R, Desrues J. Modeling the strain localization around an underground gallery with a hydro-mechanical double scale model; effect of anisotropy. *Comput Geotech*. 85(2017):384-400.
33. Chang J, Chu X, Xu Y. The role of non-coaxiality in the simulation of strain localization based on classical and cosserat continua. *Int J Numer Anal Methods Geomech*. 2017; 41:382-399.
34. Borja RI. Cam-clay plasticity. part v: a mathematical framework for three-phase deformation and strain localization analyses of partially saturated porous media. *Comput Methods Appl Mech Eng*. 2004;193(48):5301-5338.
35. Song X, Borja RI. Finite deformation and fluid flow in unsaturated soils with random heterogeneity. *Vadose Zone J*. 2014;13(5)1-11.
36. Schiava R, Etse G. Constitutive modeling and discontinuous bifurcation assessment in unsaturated soils. *J Appl Mech*. 2006;73(6):1039-1044.
37. Perić D, Zhao G, Khalili N. Strain localization in unsaturated elastic-plastic materials subjected to plane strain compression. *J Eng Mech*. (04014050):1-12 2014.
38. Song X, Wang K, Ye M. Localized failure in unsaturated soils under non-isothermal conditions. *Acta Geotech*. 2017;In print 1-13.
39. Zhang HW, Schrefler BA. Particular aspects of internal length scales in strain localization analysis of multiphase porous materials. *Comput Methods Appl Mech Eng*. 2004;193(27):2867-2884.
40. Callari C, Armero F, Abati A. Strong discontinuities in partially saturated poroplastic solids. *Comput Methods Appl Mech Eng*. 2010;199(23):1513-1535.
41. Lazari M, Sanavia L, Schrefler BA. Local and non-local elasto-viscoplasticity in strain localization analysis of multiphase geomaterials. *Int J Numer Anal Methods Geomech*. 2015;39(14):1570-1592.
42. Cao TD, Sanavia L, Schrefler BA. A thermo-hydro-mechanical model for multiphase geomaterials in dynamics with application to strain localization simulation. *Int J Numer Methods Eng*. 107:312-337 2016.
43. Choo J, White JA, Borja RI. Hydromechanical modeling of unsaturated flow in double porosity media. *Int J Geomech*. 2016;16(6):D4016002 1-18.
44. Réthoré J, Borst Rd, Abellan MA. A two-scale approach for fluid flow in fractured porous media. *Int J Numer Methods Eng*. 2007;71(7):780-800.
45. Réthoré J, De Borst R, Abellan MA. A two-scale model for fluid flow in an unsaturated porous medium with cohesive cracks. *Comput Mech*. 2008;42(2):227-238.
46. Borja RI, Song X. Strain localization in porous materials with spatially varying density and degree of saturation. *Computer Methods and Recent Advances in Geomechanics*. Oka, Murakami, Uzuoka & Kimoto, 2015, Taylor & Francis Group, London 2014:13 1-4.
47. Merry SM, Kavazanjian EJr, Fritz WU. Reconnaissance of the July 10, 2000, payatas landfill failure. *J Perform Constr Facilities*. 2005;19(2): 100-107.
48. Van Genuchten MT. A closed-form equation for predicting the hydraulic conductivity of unsaturated soils. *Soil Sci Soc Am J*. 1980;44(5):892-898.
49. White JA, Borja RI. Stabilized low-order finite elements for coupled solid-deformation/fluid-diffusion and their application to fault zone transients. *Comput Methods Appl Mech Eng*. 2008;197(49):4353-4366.
50. Choo J, Borja RI. Stabilized mixed finite elements for deformable porous media with double porosity. *Comput Methods Appl Mech Eng*. 2015;293:131-154.
51. Cervera M, Chiumenti M, Benedetti L, Codina R. Mixed stabilized finite element methods in nonlinear solid mechanics. part iii: Compressible and incompressible plasticity. *Comput Methods Appl Mech Eng*. 2015;285:752-775.
52. White JA, Borja RI. Block-preconditioned newton–krylov solvers for fully coupled flow and geomechanics. *Comput Geosci*. 2011;15(4):647-659.
53. Cervera M, Chiumenti M, Agelet de Saracibar C. Softening, localization and stabilization: capture of discontinuous solutions in j2 plasticity. *Int J Numer Anal Methods Geomech*. 2004;28(5):373-393.
54. Lewis RW, Schrefler BA. *The Finite Element Method in the Static and Dynamic Deformation and Consolidation of Porous Media*: Wiley; Chichester 1998.
55. Borja RI. On the mechanical energy and effective stress in saturated and unsaturated porous continua. *Int J Solids Struct*. 2006;43(6):1764-1786.
56. Nuth M, Laloui L. Effective stress concept in unsaturated soils: clarification and validation of a unified framework. *Int J Numer Anal Methods Geomech*. 2008;32(7):771-801.
57. Schrefler BA. The finite element method in soil consolidation: (with applications to surface subsidence). *Ph.D. Thesis*: University College of Swansea; 1984.
58. Simo JC, Hughes TJ. *Computational Inelasticity*, Vol. 7: Springer; New York 1999.
59. Bear J. *Dynamics of Fluids in Porous Media*: Dover Publications; Mineola, N.Y. 1972.

60. Liu F, Borja RI. Stabilized low-order finite elements for frictional contact with the extended finite element method. *Comput Methods Appl Mech Eng*. 2010;199(37):2456-2471.
61. Sun W, Ostien JT, Salinger AG. A stabilized assumed deformation gradient finite element formulation for strongly coupled poromechanical simulations at finite strain. *Int J Numer Anal Methods Geomech*. 2013;37(16):2755-2788.
62. Kim J, Wang W, Regueiro RA. Hybrid time integration and coupled solution methods for nonlinear finite element analysis of partially saturated deformable porous media at small strain. *Int J Numer Anal Methods Geomech*. 2015;39(10):1073-1103.
63. Taylor C, Hood P. A numerical solution of the navier-stokes equations using the finite element technique. *Comput Fluids*. 1973;1(1):73-100.
64. Babuška I. The finite element method with lagrangian multipliers. *Numer Math*. 1973;20(3):179-192.
65. Brezzi F, Bathe KJ. A discourse on the stability conditions for mixed finite element formulations. *Comput Methods Appl Mech Eng*. 1990;82(1–3):27-57.
66. Murad MA, Loula AF. On stability and convergence of finite element approximations of biot's consolidation problem. *Int J Numer Methods Eng*. 1994;37(4):645-667.
67. Bathe KJ. The inf–sup condition and its evaluation for mixed finite element methods. *Comput Struct*. 2001;79(2):243-252.
68. Boffi D, Brezzi F, Fortin M, et al. *Mixed Finite Element Methods and Applications*, Vol. 44: Springer; Berlin Heidelberg 2013.
69. Hughes TJ, Franca LP, Hulbert GM. A new finite element formulation for computational fluid dynamics: viii. the galerkin/least-squares method for advective-diffusive equations. *Comput Methods Appl Mech Eng*. 1989;73(2):173-189.
70. Hughes TJ, Feijóo GR, Mazzei L, Quincy JB. The variational multiscale method-a paradigm for computational mechanics. *Comput Methods Appl Mech Eng*. 1998;166(1–2):3-24.
71. Dohrmann CR, Bochev PB. A stabilized finite element method for the stokes problem based on polynomial pressure projections. *Int J Numer Methods Fluids*. 2004;46(2):183-201.
72. Bochev PB, Dohrmann CR, Gunzburger MD. Stabilization of low-order mixed finite elements for the stokes equations. *SIAM J Numer Anal*. 2006;44(1):82-101.
73. Truty A, Zimmermann T. Stabilized mixed finite element formulations for materially nonlinear partially saturated two-phase media. *Comput Methods Appl Mech Eng*. 2006;195(13):1517-1546.
74. Preisig M, Prévost JH. Stabilization procedures in coupled poromechanics problems: a critical assessment. *Int J Numer Anal Methods Geomech*. 2011;35(11):1207-1225.
75. Howell JS, Walkington NJ. Inf–sup conditions for twofold saddle point problems. *Numer Math*. 2011;118(4):663.
76. Hughes TJ. *The Finite Element Method: Linear Static and Dynamic Finite Element Analysis*: Dover Publications; Mineola, New York 2000.
77. Borja RI, Tamagnini C, Amorosi A. Coupling plasticity and energy-conserving elasticity models for clays. *J Geotech Geoenviron Eng*. 1997;123(10):948-957.
78. Jefferies MG. Nor-sand: a simle critical state model for sand. *Géotechnique*. 1993;43(1):91-103.
79. Andrade JE, Borja RI. Capturing strain localization in dense sands with random density. *Int J Numer Methods Eng*. 2006;67(11):1531-1564.
80. Borja RI, Song X, Rechenmacher AL, Abedi S, Wu W. Shear band in sand with spatially varying density. *J Mech Phys Solids*. 2013;61(1):219-234.
81. Gallipoli D, Gens A, Sharma R, Vaunat J. An elasto-plastic model for unsaturated soil incorporating the effects of suction and degree of saturation on mechanical behaviour.*Géotechnique*. 2003;53(1):123-136.
82. Fredlund DG, Xing A. Equations for the soil-water characteristic curve. *Can Geotech J*. 1994;31(4):521-532.
83. Masud A, Xia K. A stabilized mixed finite element method for nearly incompressible elasticity. *J Appl Mech*. 2005;72(5):711-720.
84. Hicks MA, Samy K. Influence of heterogeneity on undrained clay slope stability. *Q J Eng Geol Hydrogeol*. 2002;35(1):41-49.
85. Pan F, Ye M, Zhu J, Wu YS, Hu BX, Yu Z. Incorporating layer-and local-scale heterogeneities in numerical simulation of unsaturated flow and tracer transport. *J Contam Hydrol*. 2009;103(3):194-205.
86. Borja RI. *Plasticity Modeling & Computation*: Springer; Berlin Heidelberg 2013.
87. DE BORST R. Simulation of strain localization: a reappraisal of the cosserat continuum. *Eng Comput*. 1991;8(4):317-332.
88. Schrefler BA, Sanavia L, Majorana CE. A multiphase medium model for localisation and postlocalisation simulation in geomaterials. *Mech Cohesive-frictional Materials*. 1996;1(1):95-114.
89. Zhang HW, Sanavia L, Schrefler BA. An interal length scale in dynamic strain localization of multiphase porous media. *Mech Cohesive-frictional Materials*. 1999;4(5):443-460.
90. Zhang HW, Schrefler BA. Uniqueness and localization analysis of elastic–plastic saturated porous media. *Int J Numer Anal Methods Geomech*. 2001;25(1):29-48.